Karl L. Mitchell and Jason Rabinovitch contributed equally to this work.

Key Points:

- Recent studies on the ascent and eruption of Enceladus' plume have neglected the role of exsolution and expansion of dissolved volatiles
- Volatile-driven direct ocean-to-jet liquid water ascent is generally consistent with observations if combined with a sublimation co-plume
- This mode of ascent could preserve ocean bulk content in jets, leading to jet sampling strategies being preferred for future missions

Correspondence to:

K. L. Mitchell,
Karl.L.Mitchell@jpl.nasa.gov

A Proposed Model for Cryovolcanic Activity on Enceladus Driven by Volatile Exsolution

Karl L. Mitchell[1] , **Jason Rabinovitch[2]** , **Jonathan C. Scamardella[2]**, and **Morgan L. Cable[1]**

[1]Jet Propulsion Laboratory, California Institute of Technology, Pasadena, CA, USA, [2]Stevens Institute of Technology, Hoboken, NJ, USA

Abstract There is considerable interest in sending a mission to Enceladus to sample its erupting materials, which are sourced from its ocean, a proposed habitable environment. However, we lack resolution between competing ascent and eruption models, which offer differing consequences and challenges for mission sampling and access strategies. We report a new Enceladus ascent and eruption model, "Cryo-Erupt," where ascent from ocean to jet is driven by the exsolution and expansion of dissolved gases from ascending water within conduits. This mechanism shares many similarities with some forms of terrestrial activity, including explosive silicate volcanism, cold-water geysers and "limnic" eruptions. This preliminary study suggests that this mode of ascent and eruption is viable and broadly consistent with a range of observations including the apparent co-existence of point- (jet) and fissure- (curtain) sourced activity as well as strong contrasts in velocity and ice-to-vapor ratio between the plume and the jets feeding it. However, it requires the co-existence of a sublimation plume as an additive component to the broader plume. The outcomes of the Cryo-Erupt model differ in terms of conduit physical and chemical processes from previously proposed boiling interface eruption models, for example, predicting larger dynamic pressures and narrower conduits, which could present challenges for direct robotic access. Due to the lack of a static boiling interface or wall condensation, bulk composition is unlikely to change appreciably during ascent from the ocean-conduit interface to the jet, potentially simplifying the interpretation of samples collected in space or on Enceladus' surface.

Plain Language Summary High-speed jets from giant ice fissures on Saturn's moon Enceladus feed a large plume, which is of interest to scientists because it contains salts and organic compounds, which are evidence of a subsurface ocean that may possibly host life. However, it is unclear how the chemistry of the plume material (gas and grains) might be altered as this material moves from the ocean into space, and to what extent samples from the plume are representative of ocean composition. Previous models to predict this behavior mostly relied on boiling of water as the primary way that gas and droplets are ejected, but these models do not take into account all of the physics involved, and do not fully reproduce what Cassini observed at Enceladus. We propose a new model that instead invokes dissolved gas molecules expanding, similar to explosive volcanoes on Earth and essentially the same mechanism that causes cans of soda to explode upon opening if shaken. We predict that the erupting jets would largely preserve bulk ocean content and thus would be the best place to study ocean content, in contrast with the broader plume, which would have more water that has sublimated from the surface.

1. Introduction

One of the most striking discoveries of the Cassini-Huygens mission was the water-dominated plume erupting from the south polar terrain of Enceladus (Dougherty et al., 2006; Hansen et al., 2006; Porco et al., 2006; Spahn et al., 2006; Spencer et al., 2006; Waite et al., 2006). Multiple lines of evidence indicate that the plume is sourced from the subsurface ocean (Hsu et al., 2015; Nimmo et al., 2007; Postberg et al., 2009, 2011; Waite et al., 2017), and that this ocean may meet the conditions of a habitable environment, containing liquid water, organic chemical building blocks, and energy source(s) that could sustain metabolism (Des Marais et al., 2008; Hendrix et al., 2019). Enceladus' plume therefore provides a unique opportunity to sample material from a potentially habitable environment inside an icy moon without the need for a spacecraft to land and descend through the ice shell (e.g., Cable et al., 2021; MacKenzie et al., 2021; Reh et al., 2016). The recent observations by the James Webb Space Telescope (JWST) confirming the longevity and stability of the plume since the end of the Cassini-Huygens mission in 2017 (Villanueva, Hammel, Milam, Faggi, Glein, et al., 2023) provide further support for future missions that might sample this erupted material.

However, to draw firm conclusions about the ocean and related interior processes on Enceladus, one must quantitatively link the composition of the plume observed in space to the composition of the ocean. This presents a significant challenge, as the system is almost certainly under-constrained based on Cassini observations. It follows that any model estimating ocean composition from abundances of gas species and plume ice grain composition must rely on certain assumptions. From past studies, such assumptions are often weakly justified, for example, that (a) the excess thermal emissions from the Tiger Stripes is due to condensation and release of latent heat on the walls (Nakajima & Ingersoll, 2016), which leads to short-lived (up to months) vents that are at apparent odds with observed jet longevities (Portyankina et al., 2022), (b) the total dissolved carbonate (TDC) concentration in the salt-rich plume grains (Postberg et al., 2009, 2011) is the same as the ocean in Waite et al. (2017), and that CO_2 condenses minimally during transport through the conduit (Glein et al., 2015), which is at odds with the reported detection of CO_2 in the Tiger Stripes (Brown et al., 2006), or (c) the CO_2/H_2O ratio in the plume is the same as at the vent exit(s) (Glein & Waite, 2020), which does not account for addition of surface sublimated ice (Goguen et al., 2013) or separate venting of CO_2 (Combe et al., 2019). Until in situ measurements are made of the subsurface ocean itself, models with such assumptions are the best means of interpreting existing data and informing any future mission concepts that propose to analyze ejected Enceladus plume materials. Therefore, it is important to investigate and understand the assumptions made by existing models as well as explore models with different approaches, as the true conditions within the vents of Enceladus are not likely to fit neatly within the physics and/or chemistry described by a single modeling approach.

While the presence of salts in the E-ring (Postberg et al., 2009) informs us that not all involatile components are left behind in the Enceladus ocean, the extent to which such components are fractionated, leading to differences in relative abundances between ocean and plume, is unclear. Fractionation during ascent is indicated on the basis that erupted molecular abundances are not self-consistent with an ocean at a single pH (Section 2.2; Glein & Waite, 2020). Until recently, only a few ascent models have considered fractionation, despite the incorporation of features such as static-surface boiling (Kite & Rubin, 2016; Postberg et al., 2009; Schmidt et al., 2008), the likely consequences of which would be to enrich vapor-phase materials relative to other components in the plume. More recent models have begun to explore other aspects of chemical fractionation, such as adsorption/desorption of volatile organic compounds, indicating that certain species (such as propanol and acetic acid) may be enriched in plume grains compared to gas phase abundances, though such studies are highly dependent on limited experimental values (Bouquet et al., 2019). Furthermore, the idea that condensation onto conduit walls within Enceladus' ice shell during ascent would deplete water is assumed in Glein and Waite (2020), and adopted in more detail in Fifer et al. (2022), which is the only study to our knowledge that investigates possible bulk fractionation in detail. However, Fifer et al. (2022) relied on a single ascent and eruption model (Nakajima & Ingersoll, 2016) that features significant condensation of water onto the walls, enriching non-water components of the ocean in the plume. As noted by the authors of that work, if there were less condensation (e.g., per Kite & Rubin, 2016, or the model proposed in this work), fractionation could go in the opposite direction, and the H_2O concentration could be enriched in plume materials, diluting other constituents of interest such as potential biosignature molecules (e.g., Perera & Cockell, 2023). Until a consensus on eruption mechanics is reached, the role of fractionation is likely to remain uncertain, which presents a challenge for designing future mission concepts for Enceladus that might conduct habitability assessments or biosignature searches (e.g., Choblet et al., 2022; MacKenzie et al., 2022; Neveu et al., 2020; Reh et al., 2016; Tsou et al., 2012).

In this work, we reassess the evidence for different ascent and eruption models in the context of investigating the possibility of fractionation in the Enceladus plume. We find that no current model satisfactorily addresses all relevant physics and uniquely accounts for all observations. The differences between the models will impact fractionation during ascent, and thus confound the extent to which the jets and broader plumes sample the ocean, affecting future mission sampling strategies. We propose a new ascent model for consideration, herein referred to as Cryo-Erupt, which has a heritage from the *erupt* model (Mitchell, 2005) used in silicate volcanism. It includes physics associated with the degassing of volatile species, and attempts to produce outputs that are consistent with physical quantities of interest previously measured at Enceladus. The consequences for future mission concepts to Enceladus that involve sampling of the erupting materials are discussed.

2. Previously Proposed Enceladus Plume Models: Ascent and Eruption From Boiling

Most existing Enceladus plume transport models (Table 1; Schmidt et al., 2008; Kite & Rubin, 2016; Nakajima & Ingersoll, 2016) have assumed a boiling interface between liquid water and steam below the surface of Enceladus

Table 1
Summary of Physics Assumed in Published Enceladus Plume Transport Models

	Model					
	[A]	[B]	[C]	[D]	[E]	This work (Cryo-Erupt model)
Model assumptions						
Source of plume material: sharp boiling interface (B), volatile exsolution from liquid (L), sublimation (S)	S	B	L	B	B	L
Dissolved/exsolving volatiles considered?	Yes	No	Yes, CO_2	No	No	Yes (H_2 as proxy for multiple species)
Inclusion of compressible flow with a sonic (Mach 1) point in the conduit	No	Yes	No	Yes	No	Yes
Inclusion of salts in plume materials considered/discussed	No	Yes	Yes	Yes	Yes	Yes
Fissure (F) or discrete point sources (P) for plume	F	*	*	F	F	P
Model results						
Observed surface ice temperature distribution/heat flux matched	No	No	No	Yes	Yes	Analysis pending
Steady-state eruption and conduit geometry	Yes	*	*	No	Yes	Yes
Ice/vapor (I/V) ratio	<0.4	0.01–0.05	*	~0.1	*	~6 in jet

Note. Sources: [A] Kieffer et al. (2006), [B] Postberg et al. (2009, 2011); Schmidt et al. (2008), [C] Matson et al. (2012) [D] Ingersoll and Nakajima (2016); Nakajima and Ingersoll (2016), [E] Kite and Rubin (2016). *Not explicitly discussed.

(Figure 1—Panel A, left), and that it is this boiling process that is the primary mechanism that feeds the jets observed in space. We refer to these as "boiling models". We also use the generally accepted terminology of "jets" for the individual collimated conduit outputs that combine to form a single broader "plume" at ~40 km altitude.

One of the earliest ascent models (Schmidt et al., 2008) accounted for observations of erupted grains by considering gas flow sourced from a large subsurface void or "plume chamber". Such voids are fundamentally
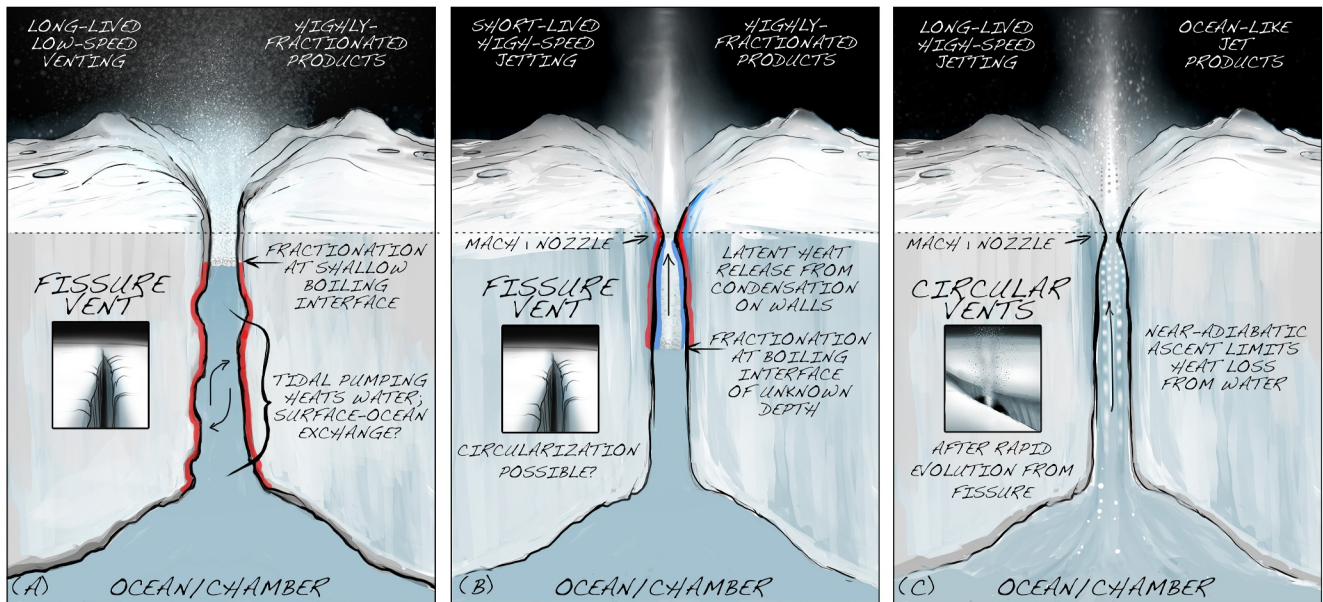
Figure 1. Understanding the conduit-vent system is critical for constraining the link between the ocean's state and the erupting jets/plume dynamics. This depiction (not to scale) illustrates key features of Enceladus ascent and eruption models that include a sharp near-surface boiling interface within a meters-wide opening (e.g., Kite & Rubin, 2016; left), a deeper boiling interface with a nozzle (e.g., Nakajima & Ingersoll, 2016; center), and the new multi-component multi-phase Cryo-Erupt model proposed in this work (right), where ascent is driven by the exsolution of volatiles. Red walls indicate areas that are actively being heated by materials in the conduit. Vent widths vary from meters (A) to centimeters (C) depending on modeling assumptions and a wide range of parameters. Ice shell thickness is likely to be many kilometers. Image Credit: NASA-JPL/Caltech Exobiology Extant Life Surveyor (EELS) team.

unstable—a fraction of ascending materials would inevitably deposit on the conduit walls, resulting in gradual closure—with no justified evolutionary pathway to form them in the first place. This issue led to models that considered progressively closing conduits with condensation of volatiles onto the walls during ascent (Nakajima & Ingersoll, 2016), providing a potential explanation for the large observed thermal anomalies. In sharp contrast, Kite and Rubin (2016) diverged considerably from that paradigm by focusing on liquid flow, with heat provided by tidal pumping preventing closure. Common characteristics of all include: (a) assumed liquid (ocean)/solid (ice wall)/gas (water vapor plume) interface, which typically necessitates that the boiling occurs at the triple point of water ($\sim$611 Pa and $\sim$273 K); (b) reliance explicitly or implicitly on complex physics (bubble bursting, particle lofting, etc.) at the boiling interface to account for observed salts, organics, and silicates in the plume (e.g., Postberg et al., 2011); and (c) neglecting the potential physical role in ascent and eruption of dissolved volatiles, such as H_2, N_2, CO_2, CO, CH_4, etc. This final feature is a major focus of this manuscript, in part because of their detection by the Cassini Ion and Neutral Mass Spectrometer or Ion Neutral Mass Spectrometer (INMS) (e.g., Peter et al., 2024; Waite et al., 2017), and in part because terrestrial dry (not involving external magma-water interactions) explosive silicate volcanism, a potential analog for the Enceladus jets, is driven by continuous exsolution/degassing and expansion of dissolved volatiles during ascent within an open conduit (e.g., Gonnerman & Manga, 2013).

We critically review some of the observations and interpretations that led to the support of the boiling models below. We then discuss a possible alternative in Section 3.

### 2.1. The Presence of Salts in the E-Ring

Observations of Saturn's E-ring (Postberg et al., 2009), which is fed from Enceladus' plume, revealed ocean-like concentrations of sodium salts (0.5%–2.0% by mass, cf. $\sim$3.5% for Earth's oceans), implying that water droplets were ejected or lofted to escape velocity (>239 m/s). However, where boiling or sublimation occurs, involatile solutes such as sodium chloride come out of solution and are only lofted if there is sufficient drag. Postberg et al. (2009, 2011) acknowledged this, and proposed a bubble-bursting mechanism to add a salty spray into the boiling eruption column. However, no analysis was presented to demonstrate that it is possible to account for such a high percentage even from a salt-saturated liquid.

2.2. Geochemical Constraints on Ocean Composition

A body of literature exists dealing with geochemical constraints on ocean composition in the context of in situ measurements performed by the Cassini spacecraft (Postberg et al., 2009; Hsu et al., 2015; Waite et al., 2017; Glein & Waite, 2020; Cable et al., 2021; and references therein). We do not review these in their entirety but instead summarize their findings that the observed and modeled ratios of plume materials are not currently consistent with any realistic unaltered ocean composition, although we note that efforts to invert the INMS data in particular are challenging and ongoing, as there may be multiple combinations of data that appear to fit the data equally well (Peter et al., 2024). Specifically, CO_2 abundances are far greater than easily supported by the alkaline pH (typically >8.5; Postberg et al., 2009; Hsu et al., 2015; Glein et al., 2015; Waite et al., 2017; Peter et al., 2024) implied by the abundance of NH_3. This has been used to support models that result in enrichment of non-H_2O vapors including CO_2 during ascent. However, fractionation during ascent within a conduit is not the only way to explain this observation. Alternatives include: (a) The lower conduit samples one zone or layer of the ocean that itself might be distinctive from the rest due to circulation (e.g., Lobo et al., 2021), convection (e.g., Vance & Brown, 2005), and the lower-than-typical pressure expected at the base of the thinned ice shell; and (b) CO_2 could exist in the form of clathrates in the ice shell that are outgassed via destabilization due to changing local pressures or temperatures resulting from eruptive activity (Combe et al., 2019).

Another point of note is that the INMS data included anomalously high mass 2 amu (H_2) levels in some parts of the plume (Waite et al., 2017). These spikes are difficult to attribute to plume spatial structure, which would require changes in H_2 density of one to two orders of magnitude within a 1-km spatial extent (or 0.1 s in duration) parallel to the spacecraft trajectory. Possible explanations (Waite et al., 2017) for the spikes include intermolecular collisions and scattering of ambient H_2 off of H_2O gas/grain jets, or H_2 scattering from stream-stream interactions between multiple gas jets, but it remains unresolved how their production should be modeled, and so they were discarded as outliers and not included in the ocean composition proposed by Waite et al. (2017). Nonetheless, these spikes constitute approximately half of the observed 2 amu counts, pointing to the possibility
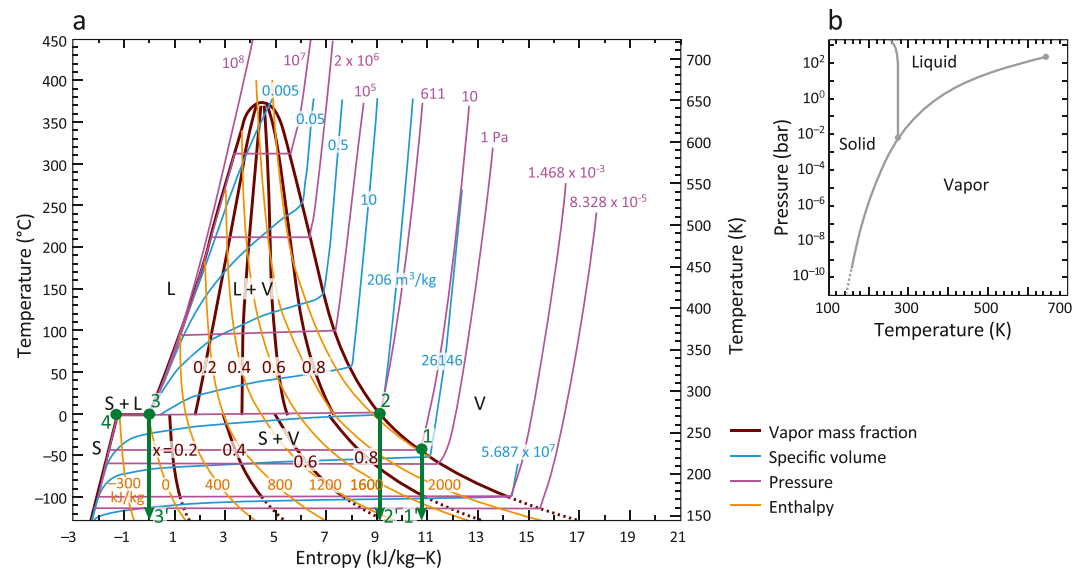
Figure 2. (a) Temperature-entropy phase diagram of water, illustrating isentropic jet expansion pathways for sublimation (1–1′), boiling (2–2′) and "cryovolcanic" (3–3′) eruption models, highlighting that cryovolcanic liquid ascent results in higher jet ice:vapor ratios than the alternatives. Insert (b) shows the phase diagram in pressure-temperature space for context. Modified from Lu and Kieffer (2009), ©2009, with permission from Elsevier.

of unexplained phenomena associated with H_2 that is unaccounted for in current models, further supporting the importance of investigating volatile-driven ascent and eruption models. Given all these factors, we find it premature to use these data to conclude in favor of any one ascent and eruption model.

2.3. A Problem of Too Much Heat

Boiling models have been favored due to their enhanced potential for heating the surrounding ice, accounting for the ~5 GW thermal anomaly observed in association with the Tiger Stripes (Spencer and Nimmo (2013)). Comparing plume model outputs to this observed thermal anomaly (e.g., Kite & Rubin, 2016; Nakajima & Ingersoll, 2016) is one way to discern if Enceladus eruption models are consistent with observations. This assumes that the observed thermal anomaly is sourced solely from the internal energy of the erupting mixture, which, if the mixture is in the gas phase, allows for considerably greater release of latent heat compared to that from a liquid mixture. With the observed eruption mass flux of ~300 kg/s (Hansen et al., 2020) which was recently confirmed in JWST observations (Villanueva, Hammel, Milam, Faggi, Glein, et al., 2023), this value is ~900 MW assuming a water vapor composition (given enthalpy of vapor deposition of ~2,800 kJ/kg at 0°C—Figure 2, difference between points 2 and 4), but only ~100 MW for a liquid water composition (given enthalpy of fusion of 334 kJ/kg at 0°C—Figure 2, difference between points 3 and 4). Thus, while ascending water vapor is technically capable of releasing more energy that could warm the ice near the Tiger Stripes, it is far from sufficient to match the observed thermal anomaly.

Three alternative explanations exist that could account for the entire thermal anomaly: (a) present-day shear heating at the Tiger Stripes focuses tidal dissipation (Nimmo et al., 2007); (b) viscous dissipative heating due to tidal pumping of water up-and-down the fissures (Kite & Rubin, 2016); or (c) supply of heat from rising water (liquid or vapor), most of which fully freezes during ascent (Ingersoll & Nakajima, 2016; Nakajima & Ingersoll, 2016), and thus the erupted flux at the surface is far less than the influx into the fissures at depth. While the first of these explanations operates independently of the eruption mechanism, the latter two are intricately intertwined with the eruption mechanism itself and are discussed in more detail below.

Tidal pumping: A variant of the boiling models was presented by Kite and Rubin (2016), who assumed an open fracture geometry with tidal pumping of the water up and down the conduit fracture. This enhances viscous dissipation, effectively focusing tidal dissipative heating on the conduit itself, more than compensating for any heat loss due to gas expansion or conduction through walls. However, because the exposed boiling cross-sectional

areas are so large, the resulting eruption would have extremely low jet densities, limiting the ability of the plume to accelerate much beyond thermal velocities ($u_{rms} \sim 615$ m/s, from Maxwell-Boltzmann distribution of water at $T = 273$ K) and accelerate large particles. While consistent with the broader plume at $\sim$600 m/s (Goldstein et al., 2018; Perry et al., 2015), we find that this is inconsistent with higher velocities associated with the collimated jets of $\sim$1.25 km/s (Perry et al., 2015), Mach 5–8 (Hansen et al., 2011), Mach $>$ 5 (Yeoh et al., 2017) and 0.8–1.8 km/s (Portyankina et al., 2022).

Wall Condensation: Isentropic or adiabatic expansion of water vapor should lead to condensation (Figure 2, path 2). The Nakajima and Ingersoll (2016) model features considerable condensation and implantation of water onto the conduit walls, significantly enhancing the transport of heat to the surrounding ice. In this model, most of the water generated at the boiling interface freezes onto the walls as it ascends, and fissures close up on the order of months, and are not dynamically stable over longer time-scales. In order to produce the observed heat output, it is noteworthy that this model requires greater crack lengths by $\sim$1.7$\times$ than the observed Tiger Stripes, which was recently revised to 2–6$\times$ by Pankine (2023) who proposed that each Tiger Stripe (or sulcus) consists of multiple parallel fractures. Ingersoll et al. (2020) showed sequences of images where some jets appear to turn off as evidence to support the model, and Teolis et al. (2017) found that they needed to include time variability for the characteristics of individual jets in order to re-create in situ observations. This contrasts with the apparent multi-year stability of many (37) individual jets reported by Portyankina et al. (2022), each of which implies quasi-steady activity and longevity of years, as well as the confirmed multi-decade longevity of the plume as a whole by JWST (Villanueva, Hammel, Milam, Faggi, Glein, et al., 2023). This assumption of massive condensation has been quantitatively incorporated into models that use plume measurements to predict ocean composition (Fifer et al., 2022; Glein & Waite, 2020), and it should be noted that the ocean compositions reported in these studies are only relevant if there is a significant amount of condensation onto conduit walls during ascent toward the surface of Enceladus.

2.4. Jet and Plume Ice-To-Vapor Ratios

The observed low ice-to-vapor (I/V) ratios in the plume have also been used to motivate the proposed boiling models (Kite & Rubin, 2016; Postberg et al., 2009; Schmidt et al., 2008). While reported I/V ratios vary considerably, from 0.07 ± 0.01 (Gao et al., 2016), 0.1–0.2 (Kieffer et al., 2009), to 0.3 ± 0.1 (Porco et al., 2014), to 0.35–0.7 (Ingersoll & Ewald, 2011), they are generally consistent with a vapor-rich source which partially condenses during expansion (Figure 2, path 2–2′).

However, an I/V ratio of 6 within the jets—individual point sources that, at least in part, feed the broader plume—was reported by Porco et al. (2014), which is broadly consistent with isentropic or adiabatic expansion of liquid water (Figure 2, path 3–3′). The analysis to support this I/V ratio was not provided in the paper, and we have been unable to independently verify the result. Independent analysis at coarser resolutions from VIMS and UVIS confirm variable I/V ratios, including values of $>$1 (Hedman et al., 2018). Confirmation of an I/V of 6 for the jets alone would be challenging to reconcile with any published boiling models, pointing clearly to liquid ascent.

Another relevant factor to consider is that all previous eruption dynamical analyses have neglected the process of surface sublimation in providing additional water (mostly vapor) to the plume (Figure 2, path 1–1′). Some degree of sublimation is proposed on the basis of observed infrared emissions by the Cassini Visual and Infrared Mapping Spectrometer (VIMS) (Goguen et al., 2013), which constrain surface ice temperature within the Tiger Stripes to 197 ± 20 K. The same study estimates a sublimation flux comparable with the entire observed plume water vapor flux, 215 ± 32 kg s^{-1} at $T = 197$ K, cf. $\sim$300 kg/s observed, noting that there is considerable uncertainty due to the high sensitivity of sublimation fluxes to temperature, which in the 170–240 K temperature range approximates T^4. Other large uncertainties are not accounted for in that predicted flux, in particular those arising from the assumption that the VIMS analysis on the basis of a single observation is representative of emissive output from the entire combined length of the Tiger Stripes. In any case, we consider this sublimation contribution to be a potentially important element of the Enceladus plume.

Unfortunately, despite potentially being one of the most revealing single detectable quantities, the I/V ratio of the jets is not usefully diagnostic at present due to observational uncertainties. However, it does motivate a closer look at neglected models that predict a high I/V ratio within the jets.

Table 2
On the Basis of Ion and Neutral Mass Spectrometer Data, and to a More Limited Extent on UVIS Data, H_2, CH_4, N_2 and/or CO Are all Present in the Enceladus Plume at Abundances Comparable With or Greater Than Predicted Saturation Levels in Enceladus' Ocean (~1 MPa)

Volatile species	CO_2	CH_4	N_2	CO	H_2
Mass (amu)	44	16	28	28	2
Henry's Law Constant, H_v^{px} [atm]	1.63×10^3	3.96×10^4	9.11×10^4	5.85×10^4	7.12×10^4
Mole Fraction	0.3%–0.8% [1, 5]	0.1%–0.3% [2, 5]	<0.5% [3]	<0.64% [4, 5*]	0.4%–1.4% [1]
Mole Fraction in ocean given I/V = 6 [6]	0.04%–0.11% [1]	0.01%–0.04% [2, 5]	<0.07% [3]	<0.09% [4, 5*]	0.06%–0.20% [1]
Saturation at 1 MPa	0.6%	0.03%	0.01%	0.02%	0.014%

Note. The ~1 MPa value is estimated based on an assumed hydrostatic pressure at the top of Enceladus' ocean with a ~10 km ice thickness, an ice density of ~1,000 kg/m^3, and gravity of ~0.1 m/s^2. Sources: [1] Waite et al. (2017); [2] Bouquet et al. (2015); [3] Hansen et al. (2011); [4] Waite et al. (2011); [5] Peter et al. (2024); [6] This assumes I/V ~ 6 (dividing the previous row by 7), consistent with Porco et al. (2014), appropriate for a liquid ascent model (path 3–3′ in Figure 2). *Peter et al. (2024) find a CO mole fraction of 0.65%–0.79%, greater than Waite et al. (2011), whilst noting that the majority may be due to incidental impact fragmentation.

3. New Enceladus Plume Model Cryo-Erupt: Volatile-Driven Ascent and Eruption

We consider it crucial to incorporate the physics associated with dissolved volatiles in the subsurface liquid water ocean at Enceladus to investigate how the Enceladus plume erupts. Previously (see Table 1), few authors, with limited but notable exceptions (Crawford & Stevenson, 1988; Matson et al., 2012; Neveu et al., 2015; Yumoto et al., 2023), have considered the role of the observed volatiles in their icy world eruption models, which is the primary difference of the newly proposed Enceladus eruption model described in this section. Kieffer et al. (2006, 2009) proposed a clathrate reservoir source for the plume, with explosive (CH_4, N_2, CO_2) clathrate decomposition driving the ascent. However, their approach was found to be at odds with the presence of salts, which implies that at least some of the ascending materials have a direct ocean source. Matson et al. (2012) discussed the role of CO_2 in enabling liquid water to ascend a conduit system. However, subsequent measurements revealed that CO_2 is unlikely to be the dominant exsolving volatile (Table 2). They also assumed an intermediate sill-like plume chamber without observational evidence or discussion as to how this specific geometry would form. Despite the knowledge that volatiles play an important role in a variety of different terrestrial eruptions (e.g., Gonnerman & Manga, 2013, and references therein), and in planetary plumes (Lu & Kieffer, 2009), volatile-driven models have recently been somewhat neglected for Enceladus. In terrestrial volcanism, depending on the flow conditions, exsolving and expanding bubbles often drive the ascent of the surrounding fluids (magma) (e.g., Gonnerman & Manga, 2013). This same principle is applied here for the Enceladus plume, and the analysis presented in this paper shows that this mechanism may be of importance to ascent and eruption dynamics.

Molecular constituents (Table 2) such as CO_2, NH_3, H_2, CH_4 and various other hydrocarbons detected in situ by Cassini's INMS account for ~5%–10% of the mole fraction of the plume (Peter et al., 2024; Waite et al., 2009, 2017). As these volatiles are known to exist within the plume, they are expected to be present at some concentration in the ocean itself, and therefore may have a profound impact on the ascent and eruption dynamics. Even mildly explosive basaltic fissure eruptions on Earth feature ascent driven by volatiles such as CO_2, with volatile exsolution and expansion generating acceleration and ascent. While silicate eruptions might appear superficially to be a weak analog, on the basis of very different chemistries and rheologies, it is also known that similar processes can occur in water eruptions. For example, exsolution and expansion of CO_2 from within Lake Nyos, Cameroon, resulted in a catastrophic limnic eruption in 1986 that killed 1,746 people and countless local animals, demonstrating the dangerous ability of exsolving gases to drive explosive decompression of even low viscosity liquids such as water (Zhang, 1996, 2000). This has led to well-studied engineered degassing of Lake Nyos (Halbwachs et al., 2020). CO_2-driven cold-water geysers are also relatively common on Earth (e.g., Watson et al., 2014). For discrete explosions, a requirement is that the driving volatile exists within the water at saturated or supersaturated concentrations, allowing a change in local solubility or pressure to drive exsolution, which can potentially lead to a runaway eruption.

Classical silicate volcanic ascent and eruption degassing models imply that volatiles (mainly H_2O and CO_2) exsolve in equilibrium with solubility laws (e.g., Dixon et al., 1995). Their nucleation is driven by thermodynamic disequilibrium due to supersaturation of those volatiles. However, various lines of evidence (Gonnerman & Manga, 2013, and references therein) support that supersaturation (solution in excess of equilibrium saturation)

by up to ~100 MPa (cf. typical magma chamber pressures of 100 s of MPa) can occur in terrestrial silicate volcanism (e.g., Mangan & Sisson, 2000), resulting in deviation from equilibrium degassing. This degree of supersaturation is a result of the energy needed to increase the surface area between two fluids (newly formed bubble and magma), and is a consequence of surface tension, γ. Supersaturation is less likely to occur in fluids containing pre-existing interfaces (other bubbles, suspended crystals, sediment, etc.) or experiencing significant strain, as these both act to reduce local nucleation energy requirements.

The same physical principles apply to water-based systems, and analogies can be made to terrestrial hydrological environments where super-saturation of dissolved volatiles has been observed in water. Small degrees of supersaturation of total dissolved gas in rivers, lakes and seas under Earth's atmosphere are common, with ~110% supersaturation being quite typical (e.g., Loeks-Johnson & Cotner, 2020; Stenberg et al., 2020). Furthermore, far greater saturation levels than this are possible in relatively dynamically stable environments (e.g., Weitkamp & Katz, 1980), with extreme cases including oxygen saturation of >300% (relative to saturated equilibrium), which was found to be responsible for fish mortality in Lake Waubesa, Wisconsin in 1940 (Woodbury, 1942). Hence, we infer that supersaturation could be of comparable importance for water eruptions on Enceladus as in terrestrial silicate volcanism.

Taken together, these observations about supersaturation in analog systems put into context the saturation values presented in Table 2, which suggest that if erupted jet materials are even remotely representative of ocean composition, then some volatile components—primarily H_2 but also plausibly CH_4, N_2 and/or CO—may be significantly supersaturated in the ocean. Thus, the presence of volatiles in the plume at concentrations greater than expected for an ~1 MPa ocean on Enceladus does not necessarily require their enrichment relative to water during ascent. That being said, rationalizing these concentrations with ocean chemical models (per Section 2.2) remains an open question. As previously stated, the ocean composition proposed by Waite et al. (2017) predicts that the H_2 concentration in the ocean would be several orders of magnitude lower than what was measured in the plume. However, due to the unknowns discussed earlier which inherently drive modeling uncertainties in previously published models (e.g., H_2 anomaly in previous measurements and a range of plausible ocean compositions is given in Figure 4 of Fifer et al. (2022), which starts with the assumption of significant amounts of condensation and a boiling interface), we think it is important to start exploring the physics associated with a volatile-driven eruption mechanism for Enceladus. Moving forward, therefore, we consider both saturated volatile concentrations at assumed starting depth/pressure as well as concentrations derived from reported plume concentrations (Table 2), and note that this is not intended to be a thorough exploration of the parameter space, but an illustrative starting point.

3.1. Ascent Model Concept—Henry's Law and Conservation of Mass and Energy

We propose that it is valuable to explore the possibility that volatile-exsolution driven ascent occurs directly from ocean-to-surface at Enceladus. Such activity is more closely analogous to terrestrial basaltic volcanism than most other ascent models, and as such, we draw on work from that community to inform our approach. We use the word "melt" or "magma" to apply to either silicate magmas or ocean-sourced "cryomagmas" (such as liquid water), "rock" to apply equally to an ice shell, and "volatile" to mean any material that can exsolve from the melt and form a gas or supercritical phase that is of lower density than the melt. In addition, we apply the word "hydrostatic" equally to magmas (where magma-static is sometimes used) and "lithostatic" equally to ice shells and consider both silicate magma chambers and Enceladus' ocean to be "source reservoirs."

Presuming that a physical conduit exists between the Enceladus Ocean and the surface, we implement an approach based on terrestrial silicate conduit flow modeling to demonstrate the importance of incorporating the physics of dissolved volatile gases and the viability of this mode of ascent. Key points are summarized below, with a complete model description presented in Appendix A, and complete implementations archived online (Rabinovitch et al., 2024). While the proof-of-concept Cryo-Erupt model presented here provides a simplified model of the Enceladus conduit system, it does include basic physics associated with the dissolved volatile gases.

Mass flow rate, $\dot{m}$, is conserved, and given by:

$$\dot{m} = \rho \, u \, A \tag{1}$$

where ρ is mixture density (kg/m^3), u is the ascent velocity (m/s), and A is conduit cross-sectional area (m^2). We assume a thermally isolated system (no heat loss through conduit walls) that conserves energy, and, due to the large latent heat of fusion of water and lack of consideration of solutes that deflate the liquid also conveniently keeps the temperature constant. Internal thermodynamic energy is balanced with external (gravitational potential and kinetic) energy. Specific conservation of energy can therefore be written as:

$$\underbrace{\overset{\text{Heat}}{T\,ds} - \overset{\substack{\text{Mechanical}\\\text{work}}}{P\,dv} + \overset{\substack{\text{Chemical}\\\text{potential}}}{\sum_i \mu_i\,dN_i}}_{\substack{\text{Specific internal}\\\text{energy [J/kg]}}} + \underbrace{\overset{\text{Kinetic}}{u\,du} + \overset{\substack{\text{Gravitational}\\\text{potential}}}{g\,dz}}_{\substack{\text{Specific external}\\\text{energy [J/kg]}}} = 0, \tag{2}$$

where T is the temperature (K), s is the specific entropy (J/(kg K)), P is Pressure (Pa), v is specific volume (1/m^3), g is Enceladus' gravity ($\sim$0.113 m/s^2), z is the elevation relative to the surface (m), μ is the chemical potential (J/molecule) and N_i is the number of molecules per kg of species i. We are aware of no chemical reactions between major plume constituents that are likely to be significant within the conduit within relevant timescales (up to hours); therefore, the chemical potential is dominated by the heat of exsolution of the volatile phases, $h_{ex}dm_{ex}$, where h_{ex} is the enthalpy of solution, and dm_{ex} is the amount of gas exsolving (e.g., the mass of gas coming out of solution and undergoing a phase change). The specific internal energies of all vapor and liquid phases are calculated separately with vapor treated as an ideal gas. At the top of the conduit, the flow velocity is assumed to be Mach 1 ($M = 1$), where the Mach number is the ratio of the local flow velocity to the local speed of sound; this boundary condition is standard for compressible flow through a long duct with viscosity or for choked flow if a converging geometry section exists. We note that Nakajima and Ingersoll (2016) also prescribe a Mach 1 boundary condition at the top of their conduit. Once boundary conditions are specified at the top and bottom of the conduit, Equation 1 can be solved numerically to determine the predicted mixture and flow properties within the conduit as a function of the distance from the top of the conduit (z).

To incorporate the Mach 1 boundary condition, it is necessary to estimate the local speed of sound throughout the conduit, which, for a two-phase (e.g., liquid and gas) mixture, is typically less than either individual component; this has been previously discussed in the context of other eruptive systems (e.g., Kieffer, 1989). We adopt a commonly used simplification (Brennen, 2005; Lorenz, 2002), originally proposed in Wood (1941), where

$$c = (AB)^{-1} \tag{3}$$

in which c [m/s] is the speed of sound, $A = [\alpha\rho_g + (1-\alpha)\rho_l]^{0.5}$, and $B = [(\alpha/(\rho_g c_g^2)) + (1-\alpha)/(\rho_l c_l^2)]^{0.5}$, where α is the void (or gas volume) fraction, and ρ_g and ρ_l are the gas phase and liquid phase densities, respectively.

For the proof-of-concept results discussed in the following sections, the following constraints are assumed and simplifying assumptions are made:

- Heat loss to the surroundings is neglected, thus the system is implicitly adiabatic;
- The conduit cross-section is assumed to be constant with depth and circular, consistent with observed point source jets and observations of thermal or thermo-rheological localization in terrestrial silicate volcanism (e.g., Wylie et al., 1999);
- The model focuses on scenarios when flow below the throat is expected to be above the triple point pressure (611 Pa)—a discussion of this is provided in Appendix A;
- Calculations start at an assumed depth of 10 km, which is comparable with modeled ice thicknesses (Hemingway et al., 2018), noting that sensitivity to this assumption is low for this implementation of the Cryo-Erupt model. Additional starting depths are provided for the viscous simulations in Appendix B. Pressure at this depth is assumed to be the lithostatic pressure from the ice column added to an overpressure, if desired;
- Henry's Law for the exsolution of a single non-H$_2$O volatile (currently H$_2$ or CH$_4$) is assumed, similar to Matson et al. (2012), applied after the onset of ascent. We acknowledge that this is a significant simplification

Table 3
Summary of the Parameter Space Explored

Model input	Values
Ice column depth	[3 5 10 20 30] km
Mass flow rate (ṁ) per conduit	[0.2 0.5 1 2 5] kg/s
Mole fraction of dissolved volatile	H_2: [0.014 0.057] %
	CH_4: [0.014 0.025 0.43] %
Ocean over-pressure	[0 1 3] MPa
Throat pressure for inviscid model	[1,000 10,000] Pa

of multi-species exsolution processes. It also neglects the possibility of high degrees of supersaturation (discussed above) within the conduit.

- Results presented incorporate two initial volatile concentrations in the ocean as bounding cases: (a) the same as measured in plume vapor observations (Waite et al., 2017) corrected for assumed I/V in the jets of 6 (Table 2 "mole fraction, given I/V = 6"), per Porco et al. (2014), also approximately consistent with path 3–3′ of Figure 2; and (b) where H_2 is saturated at 1 MPa (Table 2), which is approximately hydrostatic at the arbitrarily assumed ∼10 km starting depth. Even though these volatile concentrations are greater than the ocean composition discussed in Waite et al. (2017), based on the uncertainty associated with previous models as discussed above, we propose that these results are important in communicating how exsolving volatiles of any kind may drive and affect mixture ascent;

- A linear pressure gradient is imposed on the conduit, with an assumed throat pressure (pressure at the surface) of 10 kPa or 1 kPa, and the effects of viscous dissipation, which converts kinetic energy (KE) back into heat, are not explicitly accounted for, alleviating the need to solve for conservation of momentum (see Appendix A for justification and comparison with viscous solutions);

- Flow speeds and hence maximum KE are limited by specifying a choked Mach 1 flow boundary condition at the top of the conduit;

- The entire mixture is fixed at 273 K and buffered by the latent heat of fusion and vaporization for H_2O (N.B. this is consistent with previous work (Ingersoll & Pankine, 2010) where the mixture temperature and wall temperature were found to be within 2 K); and

- Bulk flow of the erupting mixture from ocean-to-surface is assumed, with no slip velocity between the different phases: liquid water, solid water (ice) or gas-phase water (water-vapor), and gas phase H_2.

4. Results

Model outputs are summarized on the basis of several hundred runs with varying parameters (Table 3), typically set by the range of discussed values from multiple literature sources.

The mass flow rate was selected on the basis of observed jet numbers (order 100) and water mass flux (∼300 kg/s; Hansen et al., 2020) in the context that some or even most of that mass flux may be the result of sublimation (Goguen et al., 2015) rather than provided from the jets. Pressure-balanced and over-pressured (relative to lithostatic) oceans are both considered.

Due to the multi-dimensional nature of this analysis, and the nature of this paper as a proof-of-concept rather than a comprehensive analysis of parameter space, only pertinent summaries are presented here. A complete set of data outputs is archived online together with the source code (Rabinovitch et al., 2024). In addition, limited results from the model including the effects of viscosity via a conservation of momentum solution are shown in Figure 3, while additional viscous results are included in Appendix B, together with results using CH_4 as the driving volatile, which is functionally similar to H_2 as in the results presented here.

As anticipated, conduit diameter scales with mass flow rate, a direct result of mass conservation (Equation 1). Other typical behaviors are fluid ascent velocities of tens of cm/s to tens of m/s, and associated deriving conduit diameters, assuming 100 pipe-like conduits along ∼500 km of Tiger Stripes, of a few to tens of cm, as summarized in Table B1.

Perhaps less intuitive is how specific energy is repartitioned as a function of depth, as shown in Figure 4, which includes different scenarios varying both initial volatile (for H_2 and CH_4) concentration and throat pressure, highlighting the magnitudes of the different terms in the energy equation (Equation 2). The potential energy is independent of the initial condition, and is the same for all cases. Similar to terrestrial volcanism, given sufficient availability of exsolved volatiles, the Cryo-Erupt model predicts that as gas volume fractions increase, the mixture accelerates with increasing rapidity at shallower depths below the surface. However, the speed of sound of a multi-phase mixture (Figure 5), which is low at most volume fractions when compared with pure liquid or gas phases, significantly limits the amount of energy that can be converted into KE, if conduit geometry does not permit the flow to become supersonic, which in turn limits heat loss (T.ds) to far less than the latent heat of fusion of water (334 kJ/kg).
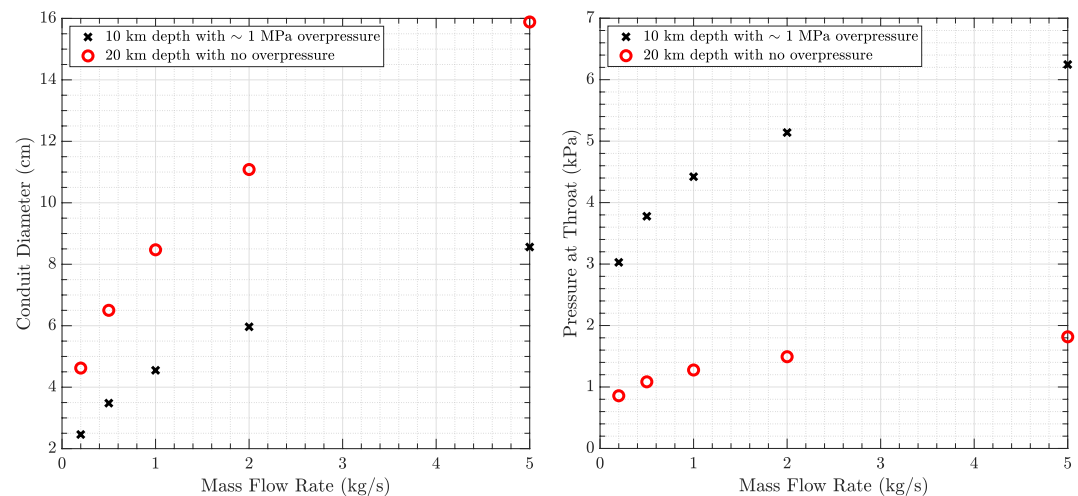
Figure 3. Conduit diameter (left) and throat pressure (right) are dependent on both mass flow rate and degree of overpressure in the source reservoir when viscosity is included. Note that mass flow rates were selected on the basis of ∼100 point source jets observed and observations of ∼300 kg/s mass flux of water (Hansen et al., 2020). Results shown for a subset of the viscous H_2 cases only.

For a given composition, the speed of sound in the throat (Figure 5) is strongly a function of throat pressure (Figures 3 and 5 right), which for the inviscid implementation is a free parameter except that it must be less than ocean pressure; Appendix B examines and justifies this relationship in more detail. Another impact of the low speed of sound for a multi-phase mixture is that the flow would have to accelerate to a higher Mach number in order to reach the Enceladus escape velocity to generate the plume observed by Cassini. In the context of the narrowly collimated jets (e.g., Hansen et al., 2020), this implies that there is likely a diverging geometrical feature through which the flow accelerates through after the throat. Such structures are a likely outcome of flow-conduit feedback that may result in descent of the choking condition during long-lived eruptions (Mitchell, 2005).

5. Discussion

The Cryo-Erupt model produces self-consistent results for all boundary conditions considered. A relatively small amount of volatile degassing—far less than the fractions observed by INMS (Waite et al., 2017)—can drive the ascent of a flow due to the early onset of nucleation and the large pressure decrease between the bottom and top of the conduit. Loss of internal heat is limited due to the low sound speed restricting increases in KE, and thus crystallization of ascending water is negligible within this adiabatic framework. In reality, it will likely be controlled by heat loss through the conduit walls, which is not dealt with explicitly here.

As previously noted, the above analysis does not consider the effects of viscosity. In reality, for activity to be sustainable, the source reservoir pressure (lithostatic/hydrostatic pressure plus overpressure) must exceed the sum of frictional and hydrostatic (or magma-static) pressure losses as well as losses associated with opening of the conduit. While these losses are typically less than in terrestrial silicate volcanism, due to water's low viscosity (see Appendix B), they can become greater if the conduit is especially narrow. Hydrostatic pressure loss is also strongly dependent on the bulk density of the fluids within the conduit, a function of both the melt and any volatiles that exsolve and expand during ascent. In the case of an erupting fluid (melt plus volatile and other inclusions) that is of greater density than surrounding rock/ice, negative buoyancy presents more of a challenge to ascent, as hydrostatic losses exceed lithostatic pressure, and so unless the reservoir is significantly overpressured—whether a magma chamber (Tait et al., 1989) or an ocean (Manga & Wang, 2007)—the role of exsolved volatiles in decreasing the effective bulk density of melts during ascent becomes more critical. In some cases, principally where volatile concentrations are significantly sub-saturated at the inlet, the assumptions of the model would be violated due to low throat pressure (Appendix B). Note, however, that we are only considering eruptions driven by exsolution and expansion of a single volatile. Integration of the effect of multiple volatiles is likely to result in increased explosivity, leading to higher pressure throat conditions and more energetic eruptions.
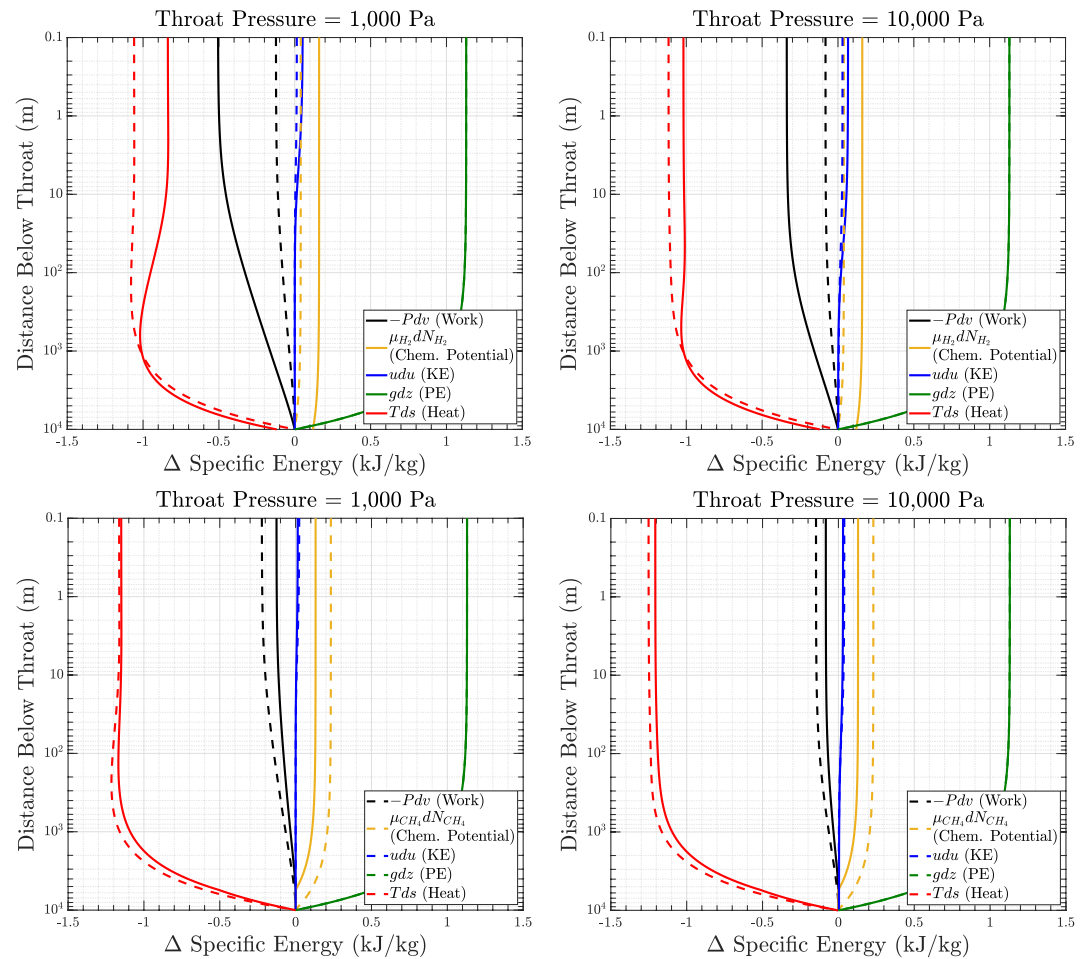
Figure 4. The Cryo-Erupt model tracks different terms from the conservation of energy and shows how energy is re-partitioned in the flow during ascent for two disparate volatile fractions and throat pressures for an assumed dissolved volatile of H_2 (top panel) and CH_4 (bottom panel). All sets of curves illustrate similar behavioral trends, with acceleration impeded by the lack of a nozzle to permit supersonic flow (Mach 1 at the top of the conduit), which also keeps changes in heat (T ds) to a minimum, consistent with very limited water phase change within the conduit. Solid lines (—) correspond to an initial mole fraction of 0.057% and 0.014% for H_2 and CH_4 respectively (see Table 2), and dashed lines (——) correspond to an initial mole fraction of 0.014% and 0.025% for H_2 and CH_4 respectively (saturation at 1 MPa).

The Cryo-Erupt model does not explicitly address the jet above the throat. However, one can infer approximate behavior of jets from this and other models via inspection of the temperature-entropy phase diagram in Figure 2. Decompression from pure liquid water, through the triple point, will result in liquid water changing phase into both solid and vapor forms at approximately the ratio of the latent heats of fusion (334 kJ/kg) and boiling (2,260 kJ/kg), representing a water I/V ratio ~6.7:1. Minor deviations from this will be primarily due to the role of non-water components. Subsequently, a supersonic jet is typically modeled to decompress isentropically, resulting in a degree of condensation of the vapor phase, slightly increasing that ratio (per Figure 2, line 3–3′). However, in the context of weakly constrained sublimation flux (Goguen et al., 2015) and mixing in the jet, we consider that an I/V ratio in the jet of ~6:1 is generally consistent with this model as well as the observationally driven findings of Porco et al. (2014).

Application of this model helps to explain some apparent observational discrepancies, such as (a) the apparent co-existence of both jet (point-source) and curtain (fissure-sourced) activity (Goldstein et al., 2018), and (b) differences in properties between the jets and broader plume discussed previously, including both supra-thermal and thermal velocities, high and low I/V ratios, and varying volatile concentrations. These may be explained by the
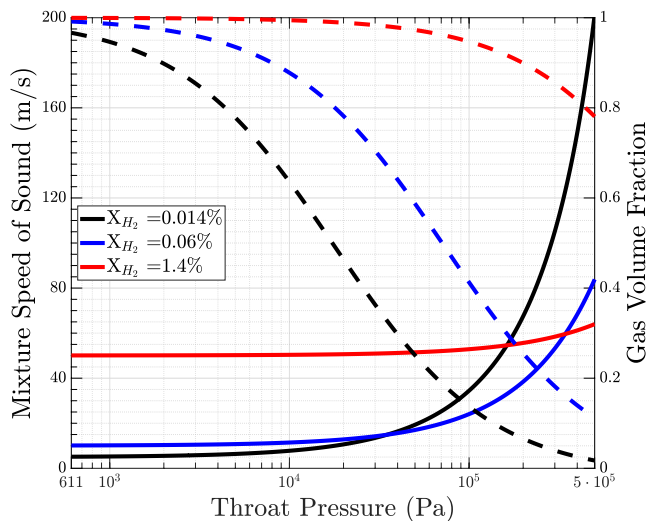
Figure 5. Multi-phase speed of sound at the throat predicted by the Cryo-Erupt model (Rabinovitch et al., 2024) for throat pressures ranging from the triple point of water, 611 Pa, to 0.5 MPa. Solid lines (−) correspond to the mixture speed of sound (left *y*-axis) at Mach 1, and dashed lines (−−) correspond to the gas volume fraction (right *y*-axis) at Mach 1. Three initial concentrations of H_2 are considered, spanning two orders of magnitude, with the upper values informed by published plume fractions from Cassini Ion a Neutral Mass Spectrometer (Waite et al., 2017).

broader plume being a mixture of both high-velocity, volatile-rich jets sourced from the ocean (this work, path 3–3′ in Figure 2), and a lower-velocity sublimation plume dominated by water vapor (path 1–1′ in Figure 2). In the context of observed surface temperatures, which imply that sublimation is occurring (Goguen et al., 2015) and may be significant relative to observed water flux (Hansen et al., 2020), such a bi-modal origin may even be preferable. However, uncertainties in the sublimation flux mean that the relative importance of the sublimation plume is unclear at this time.

It is worth considering the eruption concept presented in contrast with other models. The water-vapor-dominated sharp-boiling interface ascent models of Schmidt et al. (2008), Postberg et al. (2009, 2011) and Nakajima and Ingersoll (2016) are more consistent with near-triple-point (611 Pa) pressures around the boiling interface (required for liquid, gas and solid phases to be in equilibrium), though many Cryo-Erupt model outcomes result in mixture pressures greater than 611 Pa. For models with a boiling interface, decompression of jets is likely to approximate the path 2–2′ in Figure 2. The model of Kite and Rubin (2016), on the other hand, is more consistent with a wider open fissure in which conduit pressure is hydraulically controlled and in which boiling at the liquid surface does not result in significant back pressure or nozzle formation. We also note that, while Kieffer et al.'s (2006) approach is insufficient on its own to account for the content of the plume, path 1-1' in Figure 2 illustrates sublimation of ice, which may play an important role. The marked differences in geometric and thermodynamic parameters point toward the prospect that geophysical methods may eventually resolve between them, and we do not rule out the possibility that there may be a spectrum of eruption modes between these models. Taken together, which of the models best accounts for Enceladus' plume likely depends critically on how the ocean and related eruptive conduit systems evolve, presumably from an initial fracture, which may have different characteristics depending on whether it is upward- or downward-propagating (e.g., Hemingway et al., 2020; Rudolph et al., 2022). However it starts, given sufficient longevity, the initially planar pathway may also evolve over weeks-to-months toward more localized and pipelike geometries via thermal or thermo-rheological feedback (Wylie et al., 1999), possibly with nozzle formation and descent (Mitchell, 2005). Such evolutionary trends will be a topic of future work, but we note that such evolutionary models are incompletely developed even for more comprehensively investigated terrestrial volcanism (see e.g., Jones & Llewellin, 2021, and references therein).

6. Conclusions

We report here a new multi-component multi-phase "Cryo-Erupt" model for the plume of Enceladus, where the driving eruption mechanism is cryovolcanic—specifically, the exsolution of dissolved volatiles from the liquid water ocean during vertical ascent through conduits. We do not preclude existing models for eruption mechanisms at Enceladus with a high degree of confidence, but we note that none to date may be uniquely reconciled with all observations. We highlight the fact that most published models do not include relevant physics related to exsolving volatile gases from the ocean (Waite et al., 2017 discuss degassing from liquid water droplets before they freeze), something that is common to volcanic and geyser modeling on Earth, and therefore identify this as a key step forward in the model presented here. A feasible model that incorporates the roles of dissolved gases and sublimation has implications for mass transport within the Enceladus system and possible fractionation of sampled materials in the plume, and would hence impact future mission designs that would sample the Enceladus plume or plume material (e.g., that deposited on the surface of Enceladus, or in the E-ring).

As discussed previously, additional work is required for the Cryo-Erupt model to replicate some key characteristics more precisely, such as multi-phase exsolution. However, we propose, based on this initial analysis, that jetting activity at Enceladus may be explained using a combination of cryovolcanic ascent driven by exsolution and expansion of non-water volatiles (especially H_2, N_2, and CH_4), erupted through discrete jets emanating from the Tiger Stripes, combined with sublimation (and/or potentially declathratization) of warm ice in a way that does not require a low-pressure subsurface boiling interface. A limitation of this Cryo-Erupt model is that it alone does

not account for the excess heat observed in Enceladus' south polar region; therefore, an additional mechanism would be required. However, mechanisms do exist that provide heat independently of the rising water (e.g., Nimmo et al., 2007; Meyer et al., 2022 in review).

In terms of verifiable predictions, for the exsolution-driven ascent predicted by the Cryo-Erupt model, jet composition in space, including salts, volatiles and potential biosignature molecules (nucleic or amino acids, lipids, sugars, etc.—see Hendrix et al., 2019), is expected to be more directly representative of ocean-conduit interface composition, certainly when compared with models featuring large amounts of condensation during ascent, and probably with those featuring static boiling interfaces. This is a result of fractionation being limited due to components remaining physically coupled during ascent. However, due to the underlying assumptions, jet composition will differ significantly from broader plume composition due to the addition of vapor released by sublimation (H_2O) and incorporation of other volatiles such as CO_2 due to declathratization (Boström et al., 2021; Carrizo et al., 2022; Kieffer et al., 2006) and/or diffusive and fumarolic vapor transport processes similar to those observed in terrestrial silicate volcanism (e.g., Delmelle & Stix, 1999). While such a contrast between jet and plume is indirectly supported by apparent observed differences in ice:vapor ratio (Porco et al., 2014) and velocity (Perry et al., 2015), they are incompletely reconciled at present due to the limited and often uncertain nature of the data. This highlights the limitations of using Cassini plume measurements to constrain eruption and ocean composition, and the importance of future individual jet measurements to more directly constrain Enceladus ocean composition, and in turn its habitability and whether life may be present in that ocean today.

The conduit size, mixture composition, dynamic pressure, velocity, etc. are expected to differ significantly between boiling models and the volatile-driven Cryo-Erupt model. For example, from our analyses (Figure 3, Tables B1 and B3), it is challenging to account for throat diameter much greater than ~10-cm, so ~1 m^2 in total surface area, whereas boiling models may have far greater individual vent and total surface areas. In addition, high velocity of ascent of liquid water can result in considerable dynamic pressures. A future robotic explorer designed to descend into the conduit system beneath the surface (e.g., Carpenter et al., 2020; Ono et al., 2018) may therefore wish to take such challenges into account to enable safe passage through the conduit and direct access to ocean liquids.

Modeling efforts such as this may also lead to a deeper understanding of the role that exsolution of volatiles might play in surface-subsurface exchange on other planetary bodies. Cryovolcanic eruption of ammonia-water mixtures has been invoked to explain certain dome and pit features on Titan (Lopes et al., 2007, 2013; Mitri et al., 2008), and enclosed freezing pressurization of ammonia-water liquid has also been proposed as a mechanism for generating the Wright Mons and Piccard Mons formations at Pluto (Martin & Binzel, 2021). In addition, the recently reported endogenous CO_2 on Europa as measured by JWST is concentrated in Tara Regio, a region with geology supporting transport from this icy moon's interior (Trumbo & Brown, 2023; Villanueva, Hammel, Milam, Faggi, Kofman, et al., 2023). Future in situ observations by the Europa Clipper mission, set to arrive in the Jovian system in 2030, may shed light on whether plume activity or other processes are the primary driver of this surface deposit and possible implications for Europa's habitability (Vance et al., 2023). Improved data sets from this and other future missions as well as modeling efforts such as the "Cryo-Erupt" model proposed here that include physics associated with the degassing of volatile species will help improve our ability to peer beneath the icy crusts of these ocean worlds and constrain whether habitable conditions or life itself might be present elsewhere in the solar system.

More development work remains in order to refine the Cryo-erupt model. A requirement of this model, that ascending water does not completely freeze prior to fragmentation (the flow becoming gas-dominated) as discussed in Section 2.3, motivates coupling with an ice shell thermal model that includes sublimation and radiation to space. Such cooling may be significant, especially early on during activity before thermal gradients are established, which will reduce loss. The assumption that exsolved and expanding bubbles impart their KE to the water and drive ascent, rather than rising independently, requires further testing, and may be a critical differentiator between this work and that of Kite and Rubin (2016). A more advanced multiple species exsolution model will allow us to more accurately assess the role of observed volatiles in driving ascent. Finally, to resolve between the different models without new data, it will be necessary to consider how the ocean-conduit system evolves, especially because of the sensitivity of all of these models to geometric assumptions and source pressure.

Appendix A: Model Description, Implementation and Verification

Additional modeling details and verification results are provided in the appendix. All scripts and data to generate figures in this paper can be found in Rabinovitch et al. (2024).

A1. Model Description

We refer to the model which does not include viscosity and prescribes a linear pressure gradient to the mixture below the throat in the conduit as the "inviscid" model, whereas the model that includes viscosity is referred to as the "viscous" model. These are the two variants of the Cryo-Erupt model proposed in this work.

Both the viscous and inviscid models implemented in this work largely follow the derivations for silicate volcanic conduit flow shown in Mitchell (2005), which also follow the derivations of Mastin and Ghiorso (2000), Wilson (1980), Wilson and Head (1981), and Wilson et al. (1980). As noted in the main text we use an entropy- rather than enthalpy-focused conservation of energy due to the increased importance of latent relative to sensible heat in this water-based system, as illustrated in Figure 2. We include the pertinent information from these references in this appendix for completeness.

Conservation of mass (Equation 1) for the mixture rising through the conduit can also be written as

$$\frac{d\rho}{\rho} + \frac{du}{u} + \frac{dA}{A} = 0, \tag{A1}$$

where ρ is the mixture density, u is the mixture velocity, and A is the conduit cross-section area. For the viscous model, a constant circular cross-sectional is assumed at all depths so that $A = \pi r^2$, with r being equal to the conduit radius. Conservation of momentum can be written as

$$\rho u du + dP + F dz + \rho g dz = 0, \tag{A2}$$

where P is the static pressure, F accounts for friction in the conduit, g is the acceleration due to gravity, and z is distance below the throat. Using the same assumptions as described in Mitchell (2005), conservation of mass and momentum can be re-arranged to solve for dP/dz for a constant cross-sectional area as

$$-\frac{dP}{dz} = \frac{\rho g + F}{1 - M^2}, \tag{A3}$$

where M is the local Mach number of the mixture, defined as the local velocity divided by the local speed of sound ($M = u/c$). See Equation 3 and associated discussion in the main body of this work for assumptions and calculation
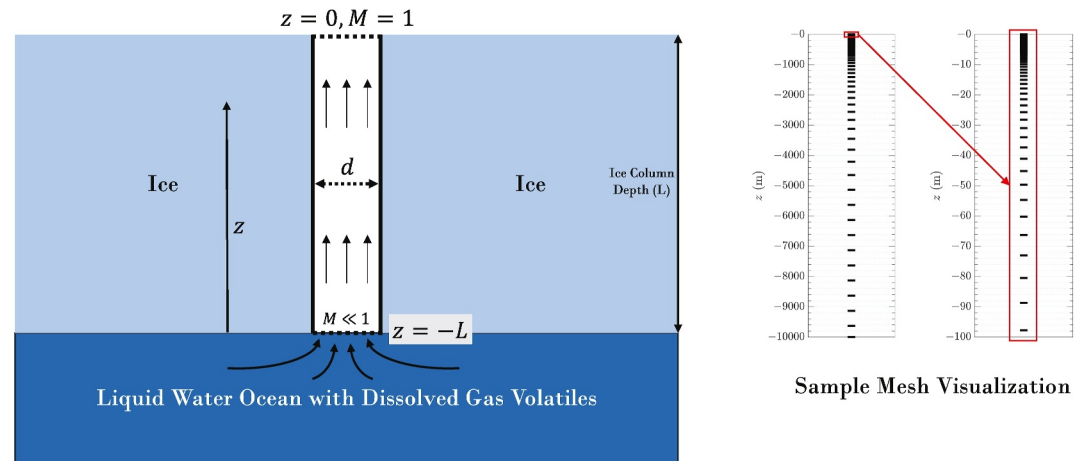
Figure A1. Model schematic (left) and sample mesh visualization (right). Every tenth point in the 1D mesh for a viscous simulation is visualized using a dash in the images on the right. The far right image shows a zoomed-in view of the mesh for the first 100 m below the surface.

Table A1
Mesh Size for Different Depths Considered for the Viscous Model

Depth (km)	nz
3	3,068
5	3,119
10	3,189
20	3,259

details for determining the mixture local speed of sound. Following Mitchell (2005) and Wilson and Head (1981), we assume $F = \frac{\rho u^2 f}{2r}$, where f, the Fanning friction factor for the circular conduit is approximated as $f = \frac{16}{Re} + f_o$. f_o is assumed to be 0.01 for the conduit following previous works (Mastin & Ghiorso, 2000; Mitchell, 2005). Re, the Reynolds number, is defined to be $Re = \frac{2\rho u r}{\mu}$, where μ is the mixture dynamic viscosity (discussed later). While not considered in this work, if a fissure geometry were to be modeled, then a similar formulation can be used with $f = \frac{24}{Re} + f_o$, and $Re = \frac{2\rho u \delta}{\mu}$, where δ is the width of the fissure (Mitchell, 2005).

Conservation of energy is discussed in the main body of this work (see Equation 2 and the surrounding discussion). In this model, we consider the following components of the mixture: liquid water (with dissolved volatile), gas-phase volatile (exsolved from liquid water), and then gas phase water (vapor) or solid phase water (ice). The amount of gas phase or solid phase water in the mixture is determined by conservation of energy (Equation 3), and specifically the Tds term.

In addition to conservation of mass, momentum, and energy, the following thermodynamic assumptions and relationships are needed. The model described in this work is isothermal with the mixture temperature held constant at 273 K. It is assumed that the Henry's law can be used for calculating the saturation mole fraction of a gas volatile species dissolved in water (no supersaturation is accounted for in the current formulation) so that the maximum mole fraction of a dissolved volatile is

$$X_{d,i} = \frac{P}{H_{v,i}^{px}},$$ (A4)

where $X_{d,i}$ is the saturation mole fraction of volatile i at pressure P. $H_{v,i}^{px}$ is Henry's Law constant for a given volatile i. We take $H_{v,H_2}^{px} = 7.1 \times 10^4$ atm and $H_{v,CH_4}^{px} = 4.0 \times 10^4$ atm in this work (calculated using NIST data (Johnson et al., 1992; NIST, 2023; Shock et al., 1989), and values are consistent with other literature sources such as Sander (2023)).

If exsolution has occurred at a given pressure, then the exsolved mole fraction of volatile (X_i) can be calculated as $X_i = X_{d,i} - X_{d_o,i}$, where $X_{d_o,i}$ is the original assumed mole fraction of dissolved volatile species i in water. The mass fraction (Y_i) of the exsolved volatile in the gas phase or the mass fraction of gas phase H_2O can be calculated as

$$Y_i = \frac{X_i M_{w,i}}{\left(X_{d_o,i} M_{w,i} + (1 - X_{d_o,i}) M_{w,H_2O}\right)},$$ (A5)

where $M_{w,i}$ is the molecular weight of species i. For a gas phase species, density can be calculated as

$$\rho_i = \frac{P}{R_i T},$$ (A6)

where R_i is the specific gas constant for species i. The specific volume, v_g, of the gas phase of the mixture, assuming ns_{gas} species, can then be calculated as

$$v_g = \sum_{i=1}^{ns_{gas}} \frac{Y_i}{\rho_i}.$$ (A7)

Similarly, the specific volume of the liquid can be expressed as $v_l = \frac{Y_{liquid}}{\rho_{liquid}}$. These values can be used to calculate the gas volume fraction, ϕ, as

$$\phi = \frac{v_g/v_l}{v_g/v_l + 1}.$$ (A8)

The density of liquid and solid H_2O components, $\rho_{H_2O,s+l}$ is defined as

$$\frac{1}{\rho_{H_2O,s+l}} = \frac{Y_{ice}}{\rho_{ice}} + \frac{Y_l}{\rho_l}, \tag{A9}$$

where the subscript l refers to liquid. Finally, the overall mixture density can be calculated as

$$\frac{1}{\rho} = \sum_{i=1}^{ns_{gas}} \frac{Y_i}{\rho_i} + \frac{Y_{i,l}}{\rho_{i,l}} + \frac{Y_{H_2O,s+l}}{\rho_{H_2O,s+l}}, \tag{A10}$$

where $Y_{i,l}$ is the dissolved mass fraction of volatile i, and $\rho_{i,l}$ is the density of volatile i in the liquid phase. While the second term on the right-hand side of Equation A10 is an over-simplification to account for the effect of the dissolved volatile on the liquid density (this term treats the dissolved volatile as a liquid immiscible with water), due to the small mass fractions assumed in this work, this term has a negligible effect on the liquid density. In future versions of the model, we expect to have a more rigorous treatment for the calculation of the liquid density. We assume $\rho_{H_2,l} = 70.85$ kg/m^3 and $\rho_{CH_4,l} = 422$ kg/m^3, and we assume that the viscosity of the mixture is dominated by the liquid phase until the gas volume fraction is greater than 75%, implying that:

$$\mu = \begin{cases} \mu_{liquid}, & \phi \le 0.75 \\ \mu_{volatile}, & \phi > 0.75 \end{cases}. \tag{A11}$$

Gas viscosities at 273 K are taken to be $\mu_{H_2} = 0.84 \times 10^{-5}$ Pa s, $\mu_{CH_4} = 1.03 \times 10^{-5}$ Pa s, and the viscosity of liquid water is taken to be $\mu_{H_2O} = 0.0018$ Pa s.

For conservation of energy (Equation 2), all calculations use stationary water at the pressure at the base of the conduit with no volatiles exsolved as the reference state. For gas phases, Pdv is integrated using the ideal gas law as $\sum_{i=1}^{ns_{gas}} Y_i R_i T \ln\left(\frac{P_o}{P}\right)$, where R_i is the specific gas constant for gas species i, and P_o is the reference pressure. For water in the liquid phase, the isothermal bulk modulus is introduced ($B = \rho \frac{dP}{d\rho}\big|_T$). The Pdv term for liquid water is first re-written as $-\frac{P}{\rho^2}d\rho$, using $v = 1/\rho$, and then the bulk modulus is introduced to write $Pdv = -\frac{P}{\rho B} dP$. This is then integrated and multiplied by $-Y_{liquid}$ to yield $Y_{liquid} \times \frac{P^2 - P_o^2}{2 \rho B}$, where the Y_{liquid} factor is included to be consistent with calculating specific energy, and the negative sign is included to be consistent with Equation 2. The density of liquid water is assumed to be constant at 1,000 kg/m^3 and we take $B = 2.2 \times 10^9$ N/m^2. While future work could include a more detailed equation of state for the liquid water and relax the constant density assumption, we find that the contribution to the Pdv term for the exsolved volatile is much greater than that of the contribution from the liquid water, leaving the current work insensitive to this assumption in the calculation of Pdv. Furthermore, density predictions for water using the NIST database (NIST, 2023) range from ∼1,002.9 kg/m^3 at the highest pressure considered in this work, to ∼999.8 kg/m^3 near triple point conditions, further supporting the approximation of a constant liquid water density in this work. For the heat of solution in water, the following values are used for H_2 and CH_4, respectively: −5.1 kJ/mol and −16.6 kJ/mol (calculated using NIST (2023); Johnson et al., 1992; Shock et al., 1989).

From Equation 2, all terms except for the Tds term can be calculated as a function of the mixture state. Therefore, Equation 2 can simply be re-arranged as $Tds = pdv - \sum_i^{ns_{volatiles}} \mu_i dN_i - udu - gdz$. We assume that a small amount of water phase change, with either liquid water freezing into solid ice or liquid water vaporizing generating gas phase water, accounts for this Tds term. We use a linear interpolation based on the entropy values from Figure 2 at the points labeled as 2 and 4 (100% vapor and 100% solid, respectively, at 0°C and 611 Pa). If $Tds > 0$, then we approximate the mass fraction of water vapor as $Y_{H_2O,vapor} = \frac{\frac{Tds}{T}}{9.0 \text{ kJ/(kg K)}}$. Similarly, if $Tds < 0$, then we approximate the mass fraction of water vapor as $Y_{H_2O,vapor} = \frac{\frac{Tds}{T}}{-1.2 \text{ kJ/(kg K)}}$. This is an approximation, and points 2 and 4 in Figure 2 correspond to $P = 611$ Pa. The entropy values that define the solid and liquid phase boundaries are functions of pressure, but we find that due to the extremely small amount of gas phase or solid phase that is generated in our models, our results are not sensitive to this simplification. In fact, while our implementation is generalized for both gas phase and solid phase (ice) water, we find that in all simulations, we

only observe the formation of solid phase water, and the mass fraction is always <1% in the simulations considered. We also neglect the volume of the solid ice particles in the mixture volume fraction calculations.

A2. Model Implementation

For the numerical implementation of the two models, the primary difference between the viscous and inviscid models is whether pressure is determined or imposed throughout the conduit. In the inviscid model, a linear pressure gradient is imposed between an assumed static pressure at the top of the conduit (sonic point) and an assumed pressure at the base of the conduit. However, in the viscous model, Equation A3 is used to determine pressure. A general schematic of the model is shown in Figure A1.

Once pressure is known, Equation A4 can be used to determine the amount of volatile that is in the gas phase, which then allows for the mixture speed of sound to be calculated. Therefore, once pressure is known in addition to mass flux, all other quantities can be determined iteratively based on the conservation equations described in the previous section. In this work, the Matlab function "fsolve" is used to solve these equations iteratively (solver tolerances: "FunctionTolerance", 1e−12, "OptimalityTolerance", 1e−10, "MaxIterations", 1,000, "MaxFunctionEvaluations", 50,000—results were found to not be sensitive to solver settings) at every location in the conduit.

For the inviscid model, conditions at the top of the conduit are solved first. As pressure is known, the speed of sound can be calculated at all points in the conduit. At the top of the conduit, the speed of the mixture is equal to the local speed of sound since the top of the conduit represents a sonic point in the flow ($M = 1$). With velocity, pressure and exsolved volatile content known, all other mixture properties can be calculated. Based on the calculations performed at the surface, the quantity ρu (mass flux) can be determined. Conservation of mass for a constant area conduit implies that $\rho u = const$, and therefore this quantity (mass flux) is known for the entire conduit. This enables all mixture properties to be calculated as a function of depth. It is interesting to note that the inviscid model does not assume a conduit length scale (e.g., diameter) nor is a value for mass flow rate required.

On the contrary, for the viscous model, both a conduit radius and mass flow rate are required. In this work, we specify a mass flow rate (and all other required initial conditions—see Table A2) and iterate on conduit radius until $M = 1.000 \pm 0.001$ at the top of the conduit ($z = 0$ m). The numerical discretization (mesh) is shown in Figure A1 and results from a mesh convergence study are shown below along with additional details on the mesh generation. For the viscous model, initial conditions are specified at the base of the conduit and then we numerically solve the resulting mixture conditions stepping toward the surface. Successive iterations (full conduit simulations) where tolerances are continually increased of the Matlab function "fminbnd" are used to iterate on radius until the specified choke condition at the top of a conduit is reached for a given set of initial conditions.

For a given set of initial conditions and a conduit radius, the flow conditions at the base of the conduit can be calculated. Equation A3 is discretized using a simple explicit Euler method to calculate pressure:

$$P^{n+1} = P^n - \Delta z^n \; \frac{\rho^n g + F^n}{1 - (M^n)^2}, \tag{A12}$$

where the superscript corresponds to spatial location in the conduit with $n = 1 .. nz$, where nz is the number of points used to discretize the conduit (number of points in the mesh). We define $\Delta z^n = z^{n+1} - z^n$, and $n = 1$ corresponds to

Table A2
Parameter Space Investigated for the Viscous Model

Model input	Values
Ice column depth	[3 5 **10** 20 30] km
Mass flow rate ($\dot{m}$) per conduit	[0.2 0.5 **1** 2 5] kg/s
Mole fraction of dissolved volatile	H_2: [0.014 0.057] %
	CH_4: [0.014 0.025 0.043] %
Ocean over-pressure	[**0** 1 3] MPa

Note. That only a subset of this parameter space was run assuming CH_4 as the volatile consisting of the "baseline" model run (initial conditions in bold).
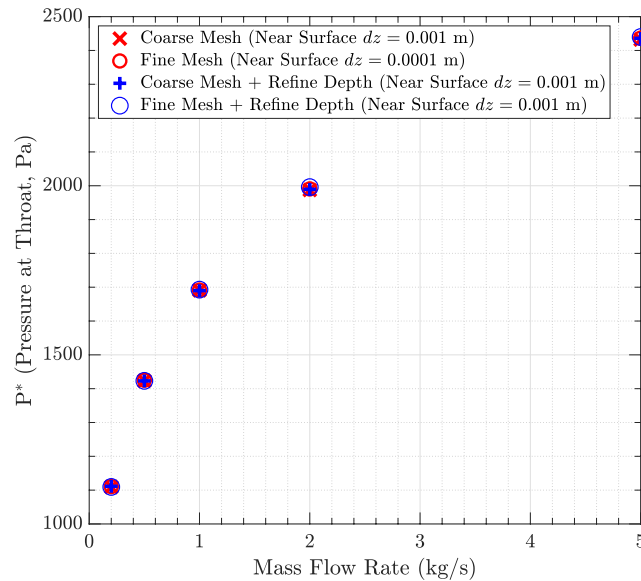
Figure A2. Static pressure at the top of the conduit as a function of mass flow rate for several different mesh resolutions. $L = 10$ km, no over-pressure, and H_2 is assumed to be the dissolved volatile with a mole fraction of 0.057%.

the base of the conduit, while $n = nz$ corresponds to the top of the conduit where $z = 0$ m. As an increasing value of n moves closer to the conduit surface, the quantity Δz is always positive, consistent with the fact that the pressure decreases as the mixture moves closer to the surface, as, theoretically, $M \leq 1$ at all points in the conduit.

If the radius of the conduit is such that the initial conditions at depth are not consistent with the mixture reaching Mach 1 at $z = 0$ m, then a new conduit radius is used until the Mach 1 criteria is met. In some cases, it was observed numerically that the Mach number would unphysically go supersonic ($M > 1$) when $z < 0$ m which would cause the sign of the second term on the right-hand side of Equation A12 to be positive. In several numerical simulations, this caused a Mach number overshoot that later converged to a sonic condition at the top of the conduit (a non-physical solution). In order to correct this, if the Mach number of the mixture started to decrease as the depth decreased that iteration would be terminated, a new radius would be chosen, and a new iteration would commence.

As the mixture travels closer to the top of the conduit, the static pressure decreases. In its current implementation, this model does not account for liquid water to water vapor phase changes that would be expected to occur if the mixture pressure drops below 611 Pa. Scenarios where pressure drops below 611 Pa at any point in the conduit are flagged. If this phase change were to be included in the model, then the pressure would be buffered by this liquid water to gas phase water phase change, which still represents a physical flow scenario. These runs are only flagged in this work because these results are not self-consistent with the model implementation. They still represent viable eruption conditions, and future work could account for this phase change.

A3. Model Verification (Mesh Description and Mesh Sensitivity Study)

As shown in Figure A1, the conduit is discretized in 1-dimension (z) with $n = 1 \, ..nz$ points. As previously stated, $n = 1$ corresponds to the base of the conduit, while $n = nz$ corresponds to the top of the conduit where $z = 0$ m. A non-constant Δz is used ($\Delta z^n = z^{n+1} - z^n$) to cluster mesh points near $z = 0$ m, which is where the highest flow gradients are expected to occur. A geometric stretching is applied near the top of the conduit such that $\frac{\Delta z^{n-1}}{\Delta z^n} = r$, where r is the mesh stretching factor. The structure of the mesh is slightly different for the viscous and inviscid simulations. This is motivated by the fact that for the inviscid simulations, where a pressure profile is prescribed a priori, the solution for any location in the conduit (z^n) is not a function of any of its surrounding points (z^{n-1} and/or z^{n+1}). As a result of this, the clustering of mesh points near the conduit surface is primarily motivated by the desire to plot smooth profiles. The mesh generation algorithm for the inviscid and viscous simulations is described below.
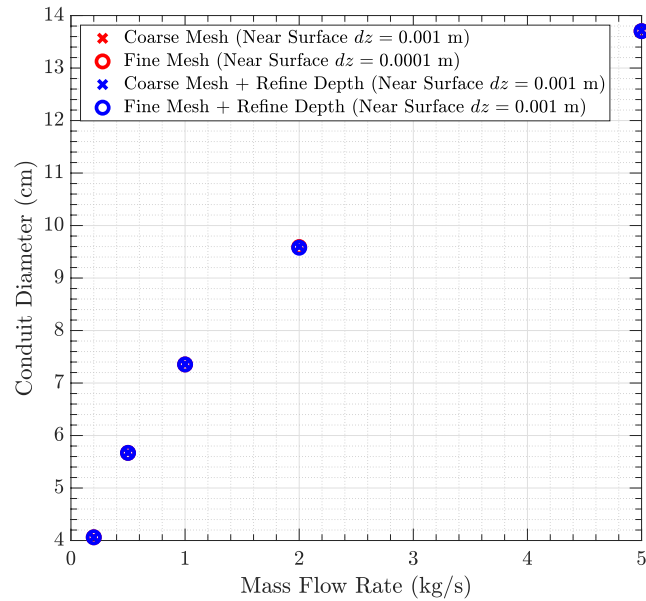
Figure A3. Conduit diameter as a function of mass flow rate for several different mesh resolutions. $L = 10$ km, no over-pressure, and H_2 is assumed to be the dissolved volatile with a mole fraction of 0.057%.

Inviscid mesh generation: At the top of the conduit, the initial mesh spacing Δz_o ($\Delta z_o = z^{nz} - n^{nz-1}$) is chosen to be 0.01 m. As the distance from the top of the conduit increases, the mesh spacing increases as $\frac{\Delta z^{n-1}}{\Delta z^n} = r$, with $r = 1.02$. This continues while $\Delta z < \frac{L}{100}$, where L is the ice column depth, and then the mesh spacing is set to a constant value of $\Delta z = \frac{L}{100}$. We set Δz^1, to a different value to ensure that the correct conduit depth is reached ($z^1 = -L$). For the 10 km depth considered for the inviscid model (based on the parameters described above), $nz = 517$.

Viscous mesh generation: This model is expected to be more sensitive to gradients near the top of the conduit when solving for the pressure as a function of depth, so a slightly different approach for the mesh generation is
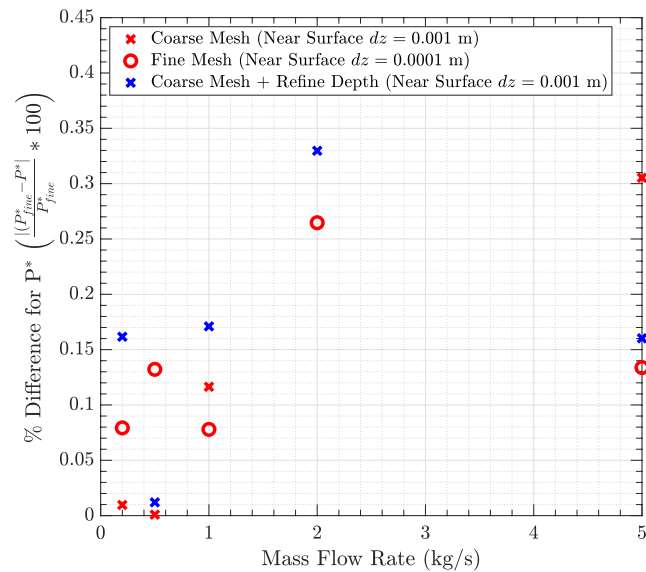
Figure A4. Variability of throat static pressure for different mesh resolutions. For all meshes considered, we observe a <0.5% difference for the different simulations. $L = 10$ km, no over-pressure, and H_2 is assumed to be the dissolved volatile with a mole fraction of 0.057%.

adopted for the viscous simulations. First, we set a region with constant mesh spacing near the top of the conduit up to a depth of h_{const}. Here we choose $\Delta z_o = 0.001$ m and $h_{const} = 2$ m. After this 2 m region with constant mesh spacing, we use the same mesh stretching technique previously described, with $r = 1.01$. This stretching is continued while $\Delta z < \frac{L}{DF}$, where DF is the Depth Factor, and we choose $DF = 200$. From this point to the base of the conduit the mesh spacing is set to a constant value of $\Delta z = \frac{L}{DF}$, and, once again, we set Δz^1 to a different value in order to ensure that the correct conduit depth is reached. For the different depths considered in the parameter study in this work for the viscous model, Table A1 shows the number of mesh points used in a single simulation.

For the viscous simulations, we investigate the sensitivity of the model results (primarily static pressure at the top of the conduit and conduit diameter) to our mesh resolution by varying Δz_o, h_{const} and DF. In Figures A2–A4, results labeled as "Coarse Mesh" use $\Delta z_o = 0.001$ m and results labeled as "Fine Mesh" use $\Delta z_o = 0.0001$ m. Results with "Refine Depth" use $h_{const} = 5$ m and $DF = 2,000$, while the other results use $h_{const} = 2$ m and $DF = 200$. All results use $r = 1.01$. The mesh sensitivity investigation is performed for a conduit depth of 10 km, 0 external pressure and an assumed volatile of H_2 with a mole fraction of 0.057%. This resulted in mesh sizes ranging from $nz = 3,189$ to $nz = 52,987$. It should be noted that mesh sensitivity study was performed with $f = \frac{24}{Re} + f_o$, though this value of the friction factor was found to have little effect on the modeling outcomes compared to $f = \frac{16}{Re} + f_o$ which was used for all other results reported in this work.

The results shown in Figure A4 show that there is a less than 0.5% difference between the static pressure at the top of the conduit for all meshes and mass flow rates considered in this analysis. It is generally found that results are more sensitive to the Mach number at $z = 0$ m compared to any sensitivity observed due to mesh resolution. This motivates the use of the "Coarse Mesh" for the parameter space investigated in this work, and also motivates the use of the tight tolerance on the desired Mach number at $z = 0$ m ($M = 1.000 \pm 0.001$) when iterating on radius size for a given set of initial conditions.

Appendix B: Viscous Model Results

In this appendix, a sample comparison between results for the viscous and inviscid models is shown, and then a summary of the results for the parameter space investigated with the viscous model is shown.

B1. Comparison Between Viscous and Inviscid Model Results

As shown in Figure 3 in the main body of the paper, the viscous model shows a good agreement with the inviscid model results. To examine the differences between the two models in more details, Figures B1 and B2 compare pressure as a function of depth for $L = 10$ km, no over-pressure, H_2 as the dissolved volatile with a mole fraction of 0.057%, and $L = 10$ km, no over-pressure, CH_4 as the dissolved volatile with a mole fraction of 0.043%, respectively.

For the cases presented in Figures B1 and B2, we see that the 1,000 Pa and 10,000 Pas inviscid model results bound the pressure of the viscous case at the top of the conduit. We do observe that the viscous results fall outside of the inviscid results for depths > ~100 m. Also, as shown in Tables B1–B5, there are viscous model results where the pressure at the top of the conduit falls between 611 and 100 Pa, which would also result in a mixture velocity at the top of the conduit that is not bounded by the inviscid model results. However, while we do observe some minor discrepancies between the two models, we do see that the reduced-order inviscid model still captures the primary physical phenomena and conclusions under investigation in this work: the contribution to eruption due to dissolved volatiles should not be ignored when modeling the Enceladus plume. The inviscid model does not require the user to iterate on conduit diameter, which greatly simplifies the model implementation. The viscous model also requires an assumption to be made for the mixture viscosity (Equation A11) along with the friction factor, which imparts additional uncertainty. For a circular conduit, the Reynolds number can be re-written as a function of mass flow rate as $Re = \frac{4\dot{m}}{\mu d}$. For our viscous simulation results, we find that our approximate Reynolds number range is $\sim 8,000 \leq Re \leq 4.5 \times 10^7$, which means that the assumption of $f_o = 0.01$ is the primary contributor to the friction factor.
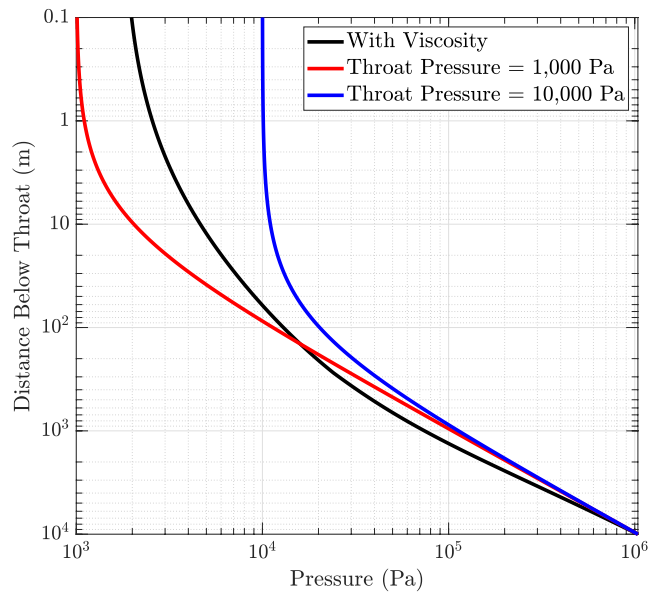
Figure B1. Comparison of static pressure in the conduit for the viscous (black) and inviscid (red, blue) models. $L = 10$ km, no over-pressure, H_2 as the dissolved volatile with a mole fraction of 0.057%.

Table B1
Summary of all H_2 Runs Where $P > 611$ Pa Everywhere in the Conduit

X_{H_2} (%)	Ice depth (km)	External pressure (MPa)	Mass flow rate (kg/s)	Conduit diameter (cm)	Pressure at throat (Pa)	Speed of sound at throat (m/s)	Column average density < ice density?	Column average density (kg/m³)
0.014	3	0	0.5	5.8	6.7e+02	5.2	Yes	8.2e+02
0.014	3	0	1.0	7.6	7.9e+02	5.2	Yes	8.2e+02
0.014	3	0	2.0	9.9	9.2e+02	5.3	Yes	8.2e+02
0.014	3	0	5.0	14.2	1.1e+03	5.3	Yes	8.2e+02
0.014	5	0	1.0	8.6	6.2e+02	5.2	Yes	8.7e+02
0.014	5	0	2.0	11.2	7.2e+02	5.2	Yes	8.7e+02
0.014	5	0	5.0	16.1	8.7e+02	5.3	Yes	8.7e+02
0.014	3	1	0.2	1.9	2.5e+03	5.7	No	9.7e+02
0.014	3	1	0.5	2.7	3.1e+03	5.9	No	9.7e+02
0.014	3	1	1.0	3.5	3.6e+03	6	No	9.7e+02
0.014	3	1	2.0	4.7	4.2e+03	6.2	No	9.7e+02
0.014	3	1	5.0	6.7	5.1e+03	6.4	No	9.7e+02
0.014	5	1	0.2	2.1	2e+03	5.6	No	9.7e+02
0.014	5	1	0.5	3.0	2.5e+03	5.7	No	9.7e+02
0.014	5	1	1.0	3.9	2.9e+03	5.8	No	9.7e+02
0.014	5	1	2.0	5.2	3.4e+03	6	No	9.7e+02
0.014	5	1	5.0	7.4	4.1e+03	6.2	No	9.7e+02
0.014	10	1	0.2	2.5	1.5e+03	5.4	No	9.7e+02
0.014	10	1	0.5	3.5	1.9e+03	5.5	No	9.8e+02
0.014	10	1	1.0	4.6	2.2e+03	5.6	No	9.8e+02
0.014	10	1	2.0	6.0	2.5e+03	5.7	No	9.8e+02

Table B1
Continued

X_{H_2} (%)	Ice depth (km)	External pressure (MPa)	Mass flow rate (kg/s)	Conduit diameter (cm)	Pressure at throat (Pa)	Speed of sound at throat (m/s)	Column average density < ice density?	Column average density (kg/m³)
0.014	10	1	5.0	8.6	3.1e+03	5.9	No	9.8e+02
0.014	20	1	0.2	2.9	1.1e+03	5.3	No	9.8e+02
0.014	20	1	0.5	4.1	1.4e+03	5.4	No	9.8e+02
0.014	20	1	1.0	5.3	1.6e+03	5.5 m/s	No	9.8e+02
0.014	20	1	2.0	7.0	1.9e+03	5.5	No	9.8e+02
0.014	20	1	5.0	10.0	2.3e+03	5.7	No	9.8e+02
0.014	30	1	0.2	3.2	8.7e+02	5.3	No	9.8e+02
0.014	30	1	0.5	4.5	1.1e+03	5.3	No	9.8e+02
0.014	30	1	1.0	5.9	1.3e+03	5.4	No	9.8e+02
0.014	30	1	2.0	7.7	1.5e+03	5.4	No	9.8e+02
0.014	30	1	5.0	11.1	1.8e+03	5.5	No	9.8e+02
0.014	3	3	0.2	1.5	4e+03	6.1	No	9.9e+02
0.014	3	3	0.5	2.1	4.9e+03	6.4	No	9.9e+02
0.014	3	3	1.0	2.8	5.7e+03	6.6	No	9.9e+02
0.014	3	3	2.0	3.7	6.6e+03	6.9	No	9.9e+02
0.014	3	3	5.0	5.3	8e+03	7.3	No	9.9e+02
0.014	5	3	0.2	1.7	3.2e+03	5.9	No	9.9e+02
0.014	5	3	0.5	2.4	4e+03	6.1	No	9.9e+02
0.014	5	3	1.0	3.1	4.6e+03	6.3	No	9.9e+02
0.014	5	3	2.0	4.1	5.4e+03	6.5	No	9.9e+02
0.014	5	3	5.0	5.9	6.5e+03	6.8	No	9.9e+02
0.014	10	3	0.2	1.9	2.4e+03	5.7	No	9.9e+02
0.014	10	3	0.5	2.8	3e+03	5.9	No	9.9e+02
0.014	10	3	1.0	3.6	3.5e+03	6	No	9.9e+02
0.014	10	3	2.0	4.7	4e+03	6.2	No	9.9e+02
0.014	10	3	5.0	6.8	4.9e+03	6.4	No	9.9e+02
0.014	20	3	0.2	2.3	1.8e+03	5.5	No	9.9e+02
0.014	20	3	0.5	3.2	2.2e+03	5.6	No	9.9e+02
0.014	20	3	1.0	4.2	2.6e+03	5.8	No	9.9e+02
0.014	20	3	2.0	5.5	3e+03	5.9	No	9.9e+02
0.014	20	3	5.0	7.9	3.7e+03	6	No	9.9e+02
0.014	30	3	0.2	2.5	1.5e+03	5.4	No	9.9e+02
0.014	30	3	0.5	3.5	1.9e+03	5.5	No	9.9e+02
0.014	30	3	1.0	4.6	2.2e+03	5.6	No	9.9e+02
0.014	30	3	2.0	6.0	2.5e+03	5.7	No	9.9e+02
0.014	30	3	5.0	8.6	3.1e+03	5.9	No	9.9e+02
0.057	3	0	0.2	3.5	1.5e+03	10	Yes	6.2e+02
0.057	3	0	0.5	4.9	1.9e+03	10	Yes	6.2e+02
0.057	3	0	1.0	6.4	2.2e+03	10	Yes	6.2e+02
0.057	3	0	2.0	8.4	2.6e+03	10	Yes	6.2e+02
0.057	3	0	5.0	12.1	3.1e+03	11	Yes	6.2e+02
0.057	5	0	0.2	3.6	1.4e+03	10	Yes	7e+02

Table B1
Continued

| X_{H_2} (%)	Ice depth (km)	External pressure (MPa)	Mass flow rate (kg/s)	Conduit diameter (cm)	Pressure at throat (Pa)	Speed of sound at throat (m/s)	Column average density < ice density?	Column average density (kg/m³)
0.057	5	0	0.5	5.1	1.8e+03	10	Yes	7e+02
0.057	5	0	1.0	6.7	2.1e+03	10	Yes	7e+02
0.057	5	0	2.0	8.7	2.4e+03	10	Yes	7.1e+02
0.057	5	0	5.0	12.5	2.9e+03	11	Yes	7.1e+02
0.057	10	0	0.2	4.0	1.2e+03	10	Yes	8e+02
0.057	10	0	0.5	5.6	1.5e+03	10	Yes	8e+02
0.057	10	0	1.0	7.3	1.7e+03	10	Yes	8e+02
0.057	10	0	2.0	9.5	2e+03	10	Yes	8e+02
0.057	10	0	5.0	13.6	2.5e+03	10	Yes	8e+02
0.057	20	0	0.2	4.6	8.6e+02	10	Yes	8.6e+02
0.057	20	0	0.5	6.5	1.1e+03	10	Yes	8.7e+02
0.057	20	0	1.0	8.5	1.3e+03	10	Yes	8.7e+02
0.057	20	0	2.0	11.1	1.5e+03	10	Yes	8.7e+02
0.057	20	0	5.0	15.9	1.8e+03	10	Yes	8.7e+02
0.057	30	0	0.2	5.4	6.2e+02	10	Yes	8.9e+02
0.057	30	0	0.5	7.6	7.9e+02	10	Yes	9e+02
0.057	30	0	1.0	10.0	9.2e+02	10	Yes	9e+02
0.057	30	0	2.0	13.0	1.1e+03	10	Yes	9e+02
0.057	30	0	5.0	18.7	1.3e+03	10	Yes	9e+02
0.057	3	1	0.2	1.9	4.8e+03	11	Yes	8.7e+02
0.057	3	1	0.5	2.8	6e+03	11	Yes	8.8e+02
0.057	3	1	1.0	3.6	7e+03	11	Yes	8.8e+02
0.057	3	1	2.0	4.8	8.1e+03	11	Yes	8.8e+02
0.057	3	1	5.0	6.8	9.8e+03	11	Yes	8.8e+02
0.057	5	1	0.2	2.2	3.9e+03	11	Yes	8.9e+02
0.057	5	1	0.5	3.1	4.9e+03	11	Yes	8.9e+02
0.057	5	1	1.0	4.0	5.7e+03	11	Yes	8.9e+02
0.057	5	1	2.0	5.2	6.6e+03	11	Yes	8.9e+02
0.057	5	1	5.0	7.5	8.1e+03	11	Yes	8.9e+02
0.057	10	1	0.2	2.5	3e+03	11	Yes	9e+02
0.057	10	1	0.5	3.5	3.7e+03	11	Yes	9e+02
0.057	10	1	1.0	4.6	4.4e+03	11	Yes	9e+02
0.057	10	1	2.0	6.0	5.1e+03	11	Yes	9e+02
0.057	10	1	5.0	8.6	6.1e+03	11	Yes	9.1e+02
0.057	20	1	0.2	2.9	2.2e+03	10	No	9.3e+02
0.057	20	1	0.5	4.1	2.8e+03	11	No	9.3e+02
0.057	20	1	1.0	5.3	3.3e+03	11	No	9.3e+02
0.057	20	1	2.0	6.9	3.8e+03	11	No	9.3e+02
0.057	20	1	5.0	9.9	4.6e+03	11	No	9.3e+02
0.057	30	1	0.2	3.2	1.8e+03	10	No	9.4e+02
0.057	30	1	0.5	4.4	2.3e+03	10	No	9.4e+02
0.057	30	1	1.0	5.8	2.7e+03	11	No	9.4e+02

Table B1
Continued

X_{H_2} (%)	Ice depth (km)	External pressure (MPa)	Mass flow rate (kg/s)	Conduit diameter (cm)	Pressure at throat (Pa)	Speed of sound at throat (m/s)	Column average density < ice density?	Column average density (kg/m³)
0.057	30	1	2.0	7.6	3.2e+03	11	No	9.4e+02
0.057	30	1	5.0	10.9	3.9e+03	11	No	9.4e+02
0.057	3	3	0.2	1.5	7.9e+03	11	No	9.5e+02
0.057	3	3	0.5	2.2	9.7e+03	11	No	9.5e+02
0.057	3	3	1.0	2.8	1.1e+04	12	No	9.5e+02
0.057	3	3	2.0	3.7	1.3e+04	12	No	9.5e+02
0.057	3	3	5.0	5.4	1.6e+04	12	No	9.5e+02
0.057	5	3	0.2	1.7	6.4e+03	11	No	9.5e+02
0.057	5	3	0.5	2.4	7.9e+03	11	No	9.5e+02
0.057	5	3	1.0	3.2	9.2e+03	11	No	9.5e+02
0.057	5	3	2.0	4.1	1.1e+04	12	No	9.5e+02
0.057	5	3	5.0	6.0	1.3e+04	12	No	9.5e+02
0.057	10	3	0.2	2.0	4.8e+03	11	No	9.5e+02
0.057	10	3	0.5	2.8	5.9e+03	11	No	9.5e+02
0.057	10	3	1.0	3.6	6.9e+03	11	No	9.5e+02
0.057	10	3	2.0	4.8	8e+03	11	No	9.5e+02
0.057	10	3	5.0	6.9	9.7e+03	11	No	9.5e+02
0.057	20	3	0.2	2.3	3.6e+03	11	No	9.6e+02
0.057	20	3	0.5	3.2	4.5e+03	11	No	9.6e+02
0.057	20	3	1.0	4.2	5.2e+03	11	No	9.6e+02
0.057	20	3	2.0	5.5	6.1e+03	11	No	9.6e+02
0.057	20	3	5.0	7.9	7.4e+03	11	No	9.6e+02
0.057	30	3	0.2	2.5	3e+03	11	No	9.7e+02
0.057	30	3	0.5	3.5	3.7e+03	11	No	9.7e+02
0.057	30	3	1.0	4.6	4.4e+03	11	No	9.7e+02
0.057	30	3	2.0	6.0	5.1e+03	11	No	9.7e+02
0.057	30	3	5.0	8.6	6.2e+03	11	No	9.7e+02

B2. Parameter Space Investigation and Summary of Viscous Results

The parameter space investigated in this work with the viscous model is summarized in Table A2. A summary of model results for these runs is reported at the end of this appendix in Tables B1–B5.

Due to the relatively large parameter space investigated, there are several ways in which the results can be visualized. However, due to the many assumptions that go into the viscous model, we do not attempt to draw detailed conclusions about conduit shape based on our results, as this work focuses on the plausibility of a volatile-driven eruption at Enceladus. However, we still show general trends based on the viscous simulation results. Figure B3 shows how the static pressure at the throat varies for cases with H_2 as the dissolved volatile with no over-pressure. In general, the cases with a lower mole fraction of H_2 are associated with a lower static pressure at the throat and a lower L/d ratio, while the high volatile concentration simulations are associated with a higher static pressure and a higher L/d ratio.

To visualize all of the viscous model results (including results that vary ocean over-pressure) that assumed H_2 as the dissolved volatile, we apply a basic dimensional analysis approach based on Buckingham's method (Bertrand, 1878; Buckingham, 1914). A description of this approach can be found in many fluid mechanics textbooks
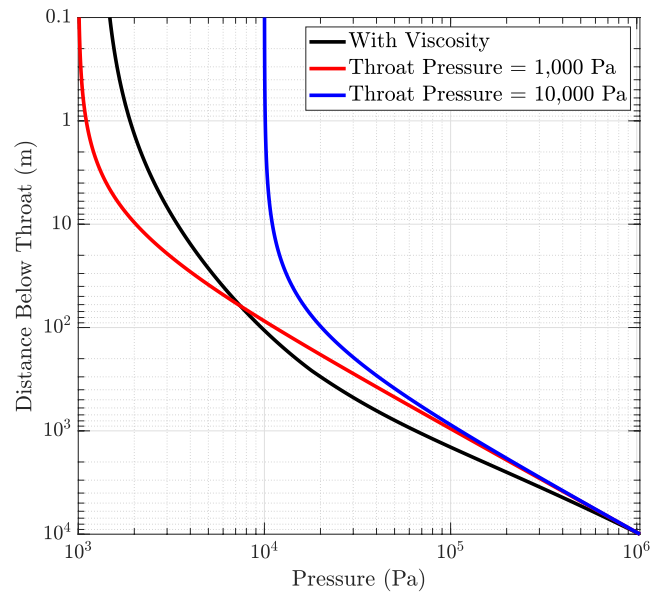
Figure B2. Comparison of static pressure in the conduit for the viscous (black) and inviscid (red, blue) models. $L = 10$ km, no over-pressure, CH_4 as the dissolved volatile with a mole fraction of 0.043%.

(e.g., Kundu et al. (2016)) and more detailed discussions pertaining to dimensional analysis can be found in Chemloul (2020), Gibbings (2014), and Szirtes (2007).

We assume that we have $n = 8$ dimensional parameters, which consist of d, the conduit diameter (the dependent variable), g, the gravitational force at Enceladus, L, the ice column depth, (H_2), the concentration of the volatile, $(H_2)_{sat}$, the saturated concentration of H_2 dissolved in water at the pressure at the base of the ice column depth (calculated from Henry's law), P_{max}, the pressure at the base of ice column (i.e., the start of the

Table B2
Summary of all H_2 Runs Where $P < 611$ Pa at any Point in the Conduit

X_{H_2} (%)	Ice depth (km)	External pressure (MPa)	Mass flow rate (kg/s)	Conduit diameter (cm)	Distance below throat where pressure <611 Pa (m)
0.014	3	0	0.2	4.1	0.054
0.014	5	0	0.2	4.7	0.6
0.014	5	0	0.5	6.6	0.11
0.014	10	0	0.2	6.9	14
0.014	10	0	0.5	9.8	11
0.014	10	0	1.0	12.8	8.6
0.014	10	0	2.0	16.9	6.7
0.014	10	0	5.0	24.4	4.4
0.014	20	0	0.2	44.0	6e+02
0.014	20	0	0.5	65.4	6e+02
0.014	20	0	1.0	88.7	6e+02
0.014	20	0	2.0	121.0	6e+02
0.014	20	0	5.0	183.6	6e+02
0.014	30	0	0.2	480.2	1.4e+03
0.014	30	0	0.5	742.3	1.4e+03
0.014	30	0	1.0	1,037.9	1.4e+03
0.014	30	0	2.0	1,455.9	1.4e+03
0.014	30	0	5.0	2,285.4	1.4e+03

Table B3
Summary of all CH$_4$ Runs Where P > 611 Pa at all Points in the Conduit

X_{CH_4} (%)	Ice depth (km)	External pressure (MPa)	Mass flow rate (kg/s)	Conduit diameter (cm)	Pressure at throat (Pa)	Speed of sound at throat (m/s)	Column average density < ice density	Column average density (kg/m^3)
0.025	10	0	1.0	9.3	7.1e+02	6.9	Yes	8.9e+02
0.025	10	0	2.0	12.1	8.2e+02	6.9	Yes	8.9e+02
0.025	10	0	5.0	17.4	1e+03	6.9	Yes	8.9e+02
0.042	10	0	0.2	4.3	8.7e+02	8.9	Yes	8.4e+02
0.042	10	0	0.5	6.0	1.1e+03	9	Yes	8.4e+02
0.042	10	0	1.0	7.8	1.3e+03	9	Yes	8.4e+02
0.042	10	0	2.0	10.2	1.5e+03	9	Yes	8.4e+02
0.042	10	0	5.0	14.7	1.8e+03	9.1	Yes	8.4e+02

conduit), ρ_{ice}, the density of the ice, and $\dot{m}$, the mass flow rate per conduit. We do not include viscosity in this analysis as we see a good collapse of the data without including the mixture viscosity, though this could be included in future work.

We therefore have four primary dimensions: mass (kg), length (m), time (s), and moles. We choose $k = 4$ repeating parameters which include all of the primary dimensions to be g (m/s^2), L (m), ρ (kg/m^3), and (H$_2$)$_{sat}$ with units (moles/m^3). This leads to $n-k = 4$ non-dimensional groups (or Pi parameters) that need to be formed. To non-dimensionalize the dependent variable, d, we take $\pi_1 = \frac{L}{d}$ (we choose this as opposed to the inverse due to the common appearance of the ratio of the length to diameter for pipe flow). We form the other three non-dimensional variables as $\pi_2 = \frac{[H_2]}{[H_2]_{sat}}$, $\pi_3 = \frac{P_{max}}{\rho g L}$, and $\pi_4 = \frac{\dot{m}}{g^{0.5}\rho L^{2.5}}$. π_2 is the ratio of supersaturation at the base of the conduit, π_3 is the ratio of ocean over-pressure at the base of the conduit (compared to lithostatic pressure) at the base of the conduit, and π_4 is a normalized mass flow rate. π_4 is related to the Froude number ($Fr = \frac{u}{\sqrt{gL}}$, the ratio of inertial forces to gravitational forces) as $\pi_4 \sim Fr \times \frac{\overline{\rho_{mixture}}}{\rho_{ice}}$, where $\overline{\rho_{mixture}}$ is the average density of the ascending mixture in the conduit, and the velocity used in the calculation of Fr is $\overline{u}$, such that $\overline{\rho_{mixture}}\,\overline{u}\,A = \dot{m}$. In the simulations (and as reported in Tables B1–B5 the ratio $\frac{\overline{\rho_{mixture}}}{\rho_{ice}}$ is $O(1)$ so π_4 is closely related to the conventional Froude number. The ratio of (average) inertial to gravitational forces may give an indication of the mixture's ability to "erupt" (and overcome gravitational forces), though it is not the objective of this paper to draw physical conclusions from the current modeling results.

The non-dimensional variables are related through $\pi_1 = f(\pi_2, \pi_3, \pi_4)$, and we assume a functional form of $f(\pi_2,\pi_3,\pi_4) = A\pi_2^a \pi_3^b \pi_4^c$. We use the Matlab function "lsqcurvefit" to fit our model results to this functional form. This allows us to solve for the parameters A, a, b, and c using a non-linear least squares data fitting algorithm. The non-dimensional data from the viscous simulation results with H$_2$ as the volatile (and pressure >611 Pa everywhere in the conduit) are shown in Figure B4, along with the coefficients determined from the fitting algorithm. In general, all the data collapse well when visualized as a function of these non-dimensional parameters. The structure of the conduit (L/d) has a weak dependence on the degree of super saturation ($a = -0.05$). This is

Table B4
Summary of all CH$_4$ Runs Where P < 611 Pa at Any Point in the Conduit

| X_{CH_4} (%)	Ice depth (km)	External pressure (MPa)	Mass flow rate (kg/s)	Conduit diameter (cm)	Distance below throat where pressure <611 Pa (m)
0.025	10	0	0.2	5.0	0.25
0.025	10	0	0.5	7.1	0.002
0.014	10	0	0.2	7.6	24
0.014	10	0	0.5	10.9	20
0.014	10	0	1.0	14.4	18
0.014	10	0	2.0	19.0	15
0.014	10	0	5.0	27.6	12

Table B5
Sample Comparisons Between H₂ and CH₄ Results

Volatile	Mole fraction of dissolved volatile (%)	Mole fraction of dissolved volatile (rationale)	Conduit diameter (cm)	Pressure at throat (Pa)	Speed of sound at throat (m/s)	Column average density (kg/m³)
H_2	0.057	Observed Concentration (min) accounting for I/V $\sim= 7$	7.3	1.7e+03	10	8e+02
CH_4	0.025	Saturated at 1 MPa	9.3	7.1e+02	6.9	8.9e+02
CH_4	0.042	Observed Concentration (max) accounting for I/V $\sim= 7$	7.8	1.3e+03	9	8.4e+02

Note. $\boldsymbol{L}$ = 10 km, 0 MPa Over-pressure, 1 kg/s Mass Flow Rate, and Varying Volatile Concentrations. Results Limited to Cases Where Throat Pressure >611 Pa

consistent with terrestrial volcanism, as exsolution within a magma source (typically a result of supersaturation) is a significant factor in eruption viability (Vergniolle, 1996), rather than eruption style. This is also consistent with observations shown in Tables B3–B7 where cases with lower mole fractions of dissolved volatile gas tend to yield results where the pressure in the conduit drops below 611 Pa (further investigation would be required to quantitatively comment on the eruption viability of cases where $P < 611$ Pa, as phase-change is not accounted for with the current modeling results). We also see that, for a given conduit length and mass flow rate, the conduit diameter is approximately proportional to $1/\sqrt{P_{max}}$. As the pressure at the base of a conduit is increased (e.g., with over-pressurization), the pressure at the top of the conduit also increases. This reduces the amount of volatile exsolution that occurs, which in turn maintains a higher mixture density. For a given mass flow rate, this results in a smaller diameter conduit from the conservation of mass. Finally, for a given conduit length, we see that the conduit diameter is approximately proportional to $\dot{m}^{0.4}$. If the mass flow rate is increased by holding pressure at the base of the conduit constant, as expected, the conduit diameter increases to accommodate the additional mass moving through the system.

The primary objective of implementing the viscous model is to justify the use of the inviscid model to demonstrate the plausibility of a volatile exsolution driven eruption mechanism for the Enceladus plume. The effect of the conduit initial conditions is investigated, and the results for the resulting conduit geometry collapse well when visualized as a function of non-dimension variables (Figure B4). Both the inviscid and viscous modeling results
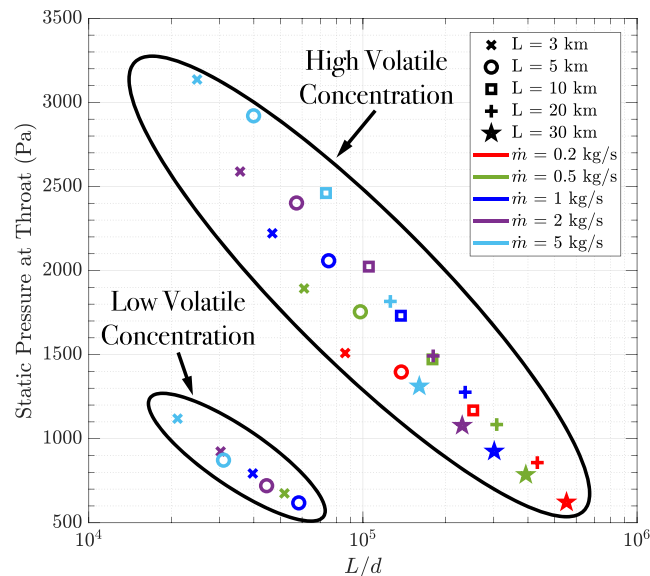
Figure B3. Static pressure at the top of the conduit as a function of conduit depth (*L*) normalized by conduit diameter (*d*). The cases visualized include no over-pressurization at the conduit base and assume H_2 as the dissolved volatile where the static pressure at the top of the conduit is > 611 Pa. Low and high volatile concentration cases refer to a mole fraction of H_2 of 0.014% and 0.057%, respectively.
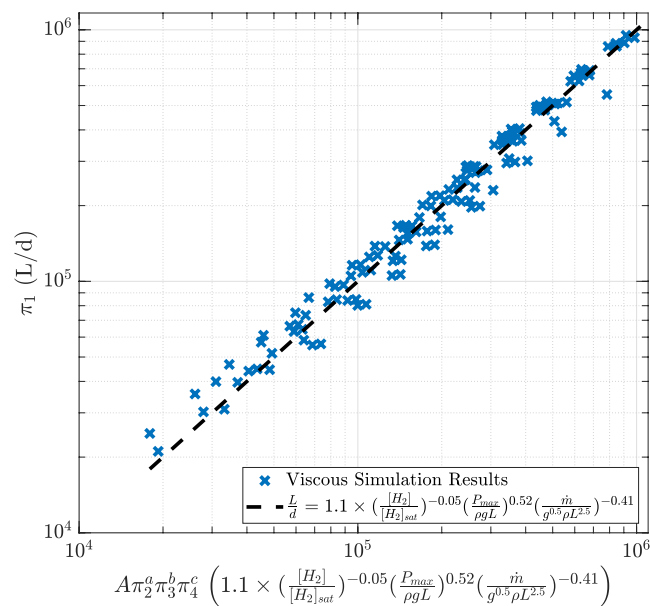
Figure B4. Non-dimensional representation of results from all viscous simulations with H_2 as the volatile where the pressure in the conduits remains >611 Pa.

support the conclusion that the physics associated volatile exsolution should be considered when modeling the Enceladus jets and resulting plume.

Data Availability Statement

All Matlab scripts (.m format), including V2 of Cryo-Erupt used for the calculations presented in this work, along with detailed results for each modeling run in Matlab data format (.mat), which serves as the data sources for Figures 3–5, Figures A2–A6, and Tables B1–B5, are available at Mendeley Data (Rabinovitch et al., 2024). They are provided under a CC BY 4.0 license. You may share, copy and modify this data set as long as you give appropriate credit, provide a link to the CC BY license, and indicate if changes were made, but you may not do so in a way that suggests the rights holder has endorsed you or your use of the data set. Note that further permission may be required for any content within the data set that is identified as belonging to a third party.

References

Bertrand, J. (1878). Sur l'homogénéité dans les formules de physique. *Comptes Rendus*, *86*(15), 916–920.

Boström, M., Esteso, V., Fiedler, J., Brevik, I., Buhmann, S. Y., Persson, C., et al. (2021). Self-preserving ice layers on CO_2 clathrate particles: Implications for Enceladus, Pluto, and similar ocean worlds. *Astronomy & Astrophysics*, *60*, A54. https://doi.org/10.1051/0004-6361/202040181

Bouquet, A., Glein, C. R., & Waite, J. H. (2019). How adsorption affects the gas-ice partitioning of organics erupted from Enceladus. *The Astrophysical Journal*, *873*(1), 28. https://doi.org/10.3847/1538-4357/ab0100

Bouquet, A., Mousis, O., Waite, J. H., & Picaud, S. (2015). Possible evidence for a methane source in Enceladus' ocean. *Geophysical Research Letters*, *42*(5), 1334–1339. https://doi.org/10.1002/2014gl063013

Brennen, C. E. (2005). *Fundamentals of multi-phase flows*. Cambridge Univ. Press.

Brown, R. H., Clark, R. N., Buratti, B. J., Cruikshank, D. P., Barnes, J. W., Mastrapa, R. M. E., et al. (2006). Composition and physical properties of Enceladus' surface. *Science*, *311*(5766), 1425–1428. https://doi.org/10.1126/science.1121031

Buckingham, E. (1914). On physically similar systems; illustrations of the use of dimensional equations. *Physical Review*, *4*(4), 345–376. https://doi.org/10.1103/physrev.4.345

Cable, M. L., Porco, C., Glein, C. R., German, C. R., MacKenzie, S. M., Neveu, M., et al. (2021). The science case for a return to Enceladus. *The Planetary Science Journal*, *2*(4), 132. https://doi.org/10.3847/psj/abfb7a

Carpenter, K., Cable, M. L., & Kornfeld, R. P. (2020). *Adapable autonomous ocean access through erupting conduits* (Vol. 2020). AGU Fall Meeting. abstract P044-0015, doi:2020AGUFMP044.0015C.

Carrizo, D., de Dios-Cubillas, A., Sánchez-García, L., & Prieto-Ballesteros, O. (2022). Interpreting molecular and isotopic biosignatures in methane-derived authigenic carbonates in the light of a potential carbon cycle in the icy moons. *Astrobiology*, *22*(5), 552–567. https://doi.org/10.1089/ast.2021.0036

Chemloul, N.-E. S. (2020). *Dimensional analysis and similarity in fluid mechanics*. Wiley-ISTE. Retrieved from https://www.wiley.com/en-us/Dimensional+Analysis+and+Similarity+in+Fluid+Mechanics-p-9781786305961

Choblet, G., Tobie, G., Buch, A., Čadek, O., Barge, L. M., Běhounková, M., et al. (2022). Enceladus as a potential oasis for life: Science goals and investigations for future explorations. *Experimental Astronomy*, *54*(2–3), 809–847. https://doi.org/10.1007/s10686-021-09808-7

Combe, J.-P., McCord, T. B., Matson, D. L., Johnson, T. V., Davies, A. G., Scipioni, F., & Tosi, F. (2019). Nature, distribution and origin of CO_2 on Enceladus. *Icarus*, *317*, 491–508. https://doi.org/10.1016/j.icarus.2018.08.007

Crawford, G. D., & Stevenson, D. J. (1988). Gas-driven water volcanism and the resurfacing of Europa. *Icarus*, *73*(1), 66–79. https://doi.org/10.1016/0019-1035(88)90085-1

Delmelle, P., & Stix, J. (1999). Volcanic gases. In H. Sigurdsson et al. (Eds.), *Encyclopedia of volcanoes* (pp. 803–815). Academic Press.

Des Marais, D. J., Nuth, J. A., Allamanola, L. J., Boss, A. P., Farmer, J. D., Hoehler, T. M., et al. (2008). The NASA astrobiology roadmap. *Astrobiology*, *8*(4), 715–730. https://doi.org/10.1089/ast.2008.0819

Dixon, J. E., Stolper, E. M., & Holloway, J. R. (1995). An experimental study of water and carbon dioxide solubilities in mid-ocean ridge basaltic liquids. Part I: Calibration and solubility models. *Journal of Petrology*, *36*, 1607–1631.

Dougherty, M. K., Khurana, K. K., Neubauer, F. M., Russell, C. T., Saur, J., Leisner, J. S., & Burton, M. E. (2006). Identification of a dynamic atmosphere at Enceladus with the Cassini Magnetometer. *Science*, *311*(5766), 1406–1409. https://doi.org/10.1126/science.1120985

Fifer, L. M., Catling, D. C., & Toner, J. D. (2022). Chemical fractionation modeling of plumes indicates a gas-rich, moderately alkaline Enceladus ocean. *The Planetary Science Journal*, *3*(8), 191. https://doi.org/10.3847/psj/ac7a9f

Gao, P., Kopparla, P., Zhang, X., Ingersoll, A. P., et al. (2016). Aggregate particles in the plumes of Enceladus. *Icarus*, *264*, 227–238. https://doi.org/10.1016/j.icarus.2015.09.030

Gibbings, J. C. (2014). *Dimensional analysis*. Springer. https://doi.org/10.1007/978-1-84996-317-6

Glein, C. R., Baross, J. A., & Waite Jr, J. H. (2015). The pH of Enceladus' ocean. *Geochimica et Cosmochimica Acta*, *162*, 202–219. https://doi.org/10.1016/j.gca.2015.04.017

Glein, C. R., & Waite, J. H. (2020). The carbonate geochemistry of Enceladus' ocean. *Geophysical Research Letters*, *47*(3), e2019GL085885. https://doi.org/10.1029/2019GL085885

Goguen, J. D., Buratti, B. J., Brown, R. H., Clark, R. N., Nicholson, P. D., Hedman, M. M., et al. (2013). The temperature and width of an active fissure on Enceladus measured with Cassini VIMS during the 14 April 2012 South Pole flyover. *Icarus*, *226*(1), 1128–1137. https://doi.org/10.1016/j.icarus.2013.07.012

Goldstein, D. B., Hedman, M., Manga, M., Perry, M., Spitale, J., & Teolis, B. (2018). Enceladus plume dynamics. In P. M. Schenk et al. (Eds.), *Enceladus and the icy moons of Saturn* (pp. 175–194). University of Arizona. https://doi.org/10.2458/azu_uapress_9780816537075-ch005

Gonnerman, H. M., & Manga, M. (2013). Dynamics of magma ascent in the volcanic conduit. In S. A. Fagents et al. (Eds.), *Modeling volcanic processes: The physics and mathematics of volanism (ch. 4)*. Cambridge University Press.

Halbwachs, M., Sabroux, J.-C., & Kayser, G. (2020). Final step of the 32-year Lake Nyos degassing adventure: Natural CO_2 recharge is to be balanced by discharge through the degassing pipes. *Journal of African Earth Sciences*, *167*, 103575. https://doi.org/10.1016/j.jafrearsci.2019.103575

Hansen, C. J., Esposito, L., Stewart, A. I. F., Colwell, J., Hendrix, A., Pryor, W., et al. (2006). Enceladus' water vapor plume. *Science*, *311*(5766), 1422–1425. https://doi.org/10.1126/science.1121254

Hansen, C. J., Esposito, L. W., Colwell, J. E., Hendrix, A. R., Portankina, G., Stewart, A. I. F., & West, R. A. (2020). The composition and structure of Enceladus' plume from the complete set of Cassini UVIS occultation observations. *Icarus*, *344*, 113461. https://doi.org/10.1016/j.icarus.2019.113461

Hansen, C. J., Shemansky, D. E., Esposito, L. W., Stewart, A. I. F., Lewis, B. R., Colwell, J. E., et al. (2011). The composition and structure of the Enceladus plume. *Geophysical Research Letters*, *38*(11), L11202. https://doi.org/10.1029/2011GL047415

Hedman, M. M., Dhingra, D., Nicholson, P. D., Hansen, C. J., Portyankina, G., Ye, S., & Dong, Y. (2018). Spatial variations in the dust-to-gas ratio of Enceladus' plume. *Icarus*, *305*, 123–138. https://doi.org/10.1016/j.icarus.2018.01.006

Hemingway, D. J., Iess, L., Tadjeddine, R., & Tobie, G. (2018). The interior of Enceladus. In P. M. Schenk et al. (Eds.), *Enceladus and the icy moons of Saturn* (pp. 57–77). The University of Arizona Press, 2018.

Hemingway, D. J., Rudolph, M. L., Manga, M., et al. (2020). Cascading parallel fractures on Enceladus. *Nature Astronomy*, *4*(3), 234–239. https://doi.org/10.1038/s41550-019-0958-x

Hendrix, A. R., Hurford, T. A., Barge, L. A., Bland, M. T., Bowman, J. S., Brinckherhoff, W., et al. (2019). The NASA roadmap to ocean worlds. *Astrobiology*, *19*, 1–27. https://doi.org/10.1089/ast.2018.1955

Hsu, H. W., Postberg, F., Sekine, Y., Shibuya, T., Kempf, S., Horanyi, M., et al. (2015). Ongoing hydrothermal activities within Enceladus. *Nature*, *519*(7542), 207–210. https://doi.org/10.1038/nature14262

Ingersoll, A. P., & Ewald, S. P. (2011). Total particulate mass in Enceladus plumes and mass of Saturn's E ring inferred from Cassini ISS images. *Icarus*, *216*(2), 492–506. https://doi.org/10.1016/j.icarus.2011.09.018

Ingersoll, A. P., Ewald, S. P., & Trumbo, S. K. (2020). Time variability of the Enceladus plumes: Orbital periods, decadal periods, and aperiodic change. *Icarus*, *344*, 113345. https://doi.org/10.1016/j.icarus.2019.06.006

Ingersoll, A. P., & Nakajima, M. (2016). Controlled boiling on Enceladus. 2. Model of the liquid-filled cracks. *Icarus*, *272*, 319–326. https://doi.org/10.1016/j.icarus.2015.12.040

Ingersoll, A. P., & Pankine, A. A. (2010). Subsurface heat transfer on Enceladus: Conditions under which melting occurs. *Icarus*, *206*(2), 594–607. https://doi.org/10.1016/j.icarus.2009.09.015

Johnson, J. W., Oelkers, E. H., & Helgeson, H. C. (1992). SUPCRT92: A software package for calculating the standard molal thermodynamic properties of minerals, gases, aqueous species, and reactions from 1 to 5000 bar and 0 to 1000°C. *Computers & Geosciences*, *18*(7), 899–947. ISSN 0098-3004. https://doi.org/10.1016/0098-3004(92)90029-Q

Jones, T. J., & Llewellin, E. W. (2021). Convective tipping point initiates localization of basaltic fissure eruptions. *Earth and Planetary Science Letters*, *553*, 116637. https://doi.org/10.1016/j.epsl.2020.116637

Kieffer, S. W. (1989). Geologic nozzles. *Review of Geophysics*, *27*(1), 3–38. https://doi.org/10.1029/rg027i001p00003

Kieffer, S. W., Lu, X., Bethke, C. M., Spencer, J. R., Marshak, S., & Navrotsky, A. (2006). A clathrate reservoir hypothesis for Enceladus' south polar plume. *Science*, *314*(5806), 1764–1766. https://doi.org/10.1126/science.1133519

Kieffer, S. W., Lu, X., McFarquhar, G., & Wohletz, K. H. (2009). A redetermination of the ice/vapor ratio of Enceladus' plumes: Implications for sublimation and the lack of a liquid water reservoir. *Icarus*, *203*(1), 238–241. https://doi.org/10.1016/j.icarus.2009.05.011

Kite, E. S., & Rubin, A. M. (2016). Sustained eruptions on Enceladus explained by turbulent dissipation in tiger stripes. *Proceedings of the National Academy of Sciences*, *113*(15), 3972–3975. https://doi.org/10.1073/pnas.1520507113

Kundu, P. K., Cohen, I. M., & Dowling, D. R. (2016). *Chapter 1 - introduction, fluid mechanics* (6th ed., pp. 1–48). Academic Press. https://doi.org/10.1016/B978-0-12-405935-1.00001-0

Lobo, A. H., Thompson, A. F., Vance, S. D., & Tharimena, S. (2021). A pole-to-equator ocean overturning circulation on Enceladus. *Nature Geoscience*, *14*(4), 185–189. https://doi.org/10.1038/s41561-021-00706-3

Loeks-Johnson, B., & Cotner, J. B. (2020). Upper Midwest lakes are supersaturated with N$_2$. *Proceedings of the National Academy of Sciences*, *117*(29), 17063–17067. https://doi.org/10.1073/pnas.1921689117

Lopes, R. M. C., Kirk, R. L., Mitchell, K. L., LeGall, A., Barnes, J. W., Hayes, A., et al. (2013). Cryovolcanism on Titan: New results from Cassini RADAR and VIMS. *JGR Planets*, *118*(3), 416–435. https://doi.org/10.1002/jgre.20062

Lopes, R. M. C., Mitchell, K. L., Stofan, E. R., Lunine, J. I., Lorenz, R., Paganelli, F., et al. (2007). Cryovolcanic features on Titan's surface as revealed by the Cassini Titan Radar Mapper. *Icarus*, *186*(2), 395–412. https://doi.org/10.1016/j.icarus.2006.09.006

Lorenz, R. D. (2002). Thermodynamics of geysers: Application to Titan. *Icarus*, *156*(1), 176–183. https://doi.org/10.1006/icar.2001.6779

Lu, X., & Kieffer, S. W. (2009). Thermodynamics and mass transport in multicomponent, multiphase H$_2$O systems of planetary interest. *Annual Review of Earth and Planetary Sciences*, *37*(1), 449–477. https://doi.org/10.1146/annurev.earth.031208.100109

MacKenzie, S. M., Neveu, M., Davila, A. F., Lunine, J. I., Cable, M. L., Phillips-Lander, C. M., et al. (2022). Science objectives for flagship-class mission concepts for the search for evidence of life at Enceladus. *Astrobiology*, *22*(6), 685–712. https://doi.org/10.1089/ast.2020.2425

MacKenzie, S. M., Neveu, M., Davila, A. F., Lunine, J. I., Craft, K. L., Cable, M. L., et al. (2021). The Enceladus Orbilander mission concept: Balancing return and resources in the search for life. *Planet. Sci. J.*, *2*, 77. https://doi.org/10.3847/psj/abe4da

Manga, M., & Wang, C.-Y. (2007). Pressurized oceans and the eruption of liquid water on Europa and Enceladus. *Geophysical Research Letters*, *34*(7), L07202. https://doi.org/10.1029/2007GL029297

Mangan, M., & Sisson, T. (2000). Delayed, disequilibrium degassing in rhyolite magma: Decompression experiments and implications for explosive volcanism. *Earth and Planetary Science Letters*, *183*(3–4), 441–455. https://doi.org/10.1016/s0012-821x(00)00299-5

Martin, C. R., & Binzel, R. P. (2021). Ammonia-water freezing as a mechanism for recent cryovolcanism on Pluto. *Icarus*, *356*, 113763. https://doi.org/10.1016/j.icarus.2020.113763

Mastin, L. G., & Ghiorso, M. S. (2000). *A numerical program for steady-state flow of magma-gas mixtures through vertical eruptive conduits*. US Geological Survey. https://apps.dtic.mil/sti/citations/ADA443634

Matson, D. L., Castillo-Rogez, J. C., Davies, A. G., & Johnson, T. V. (2012). Enceladus: A hypothesis for bringing both heat and chemicals to the surface. *Icarus*, *221*(1), 53–62. https://doi.org/10.1016/j.icarus.2012.05.031

Meyer, C. R., Buffo, J. J., Nimmo, F., Wells, A. J., Boury, S., Tomlinson, T. C., et al. (2022). A mushy sources for the geysers of Enceladus. *Earth and Planetary Astrophysics*. https://arxiv.org/abs/2208.06714

Mitchell, K. L. (2005). Coupled conduit flow and shape in explosive volcanic eruptions. *Journal of Volcanology and Geothermal Research*, *143*(1–3), 187–203. https://doi.org/10.1016/j.jvolgeores.2004.09.017

Mitri, G., Showman, A. P., Lunine, J. I., & Lopes, R. M. C. (2008). Resurfacing of Titan by ammonia-water cryomagma. *Icarus*, *196*(1), 216–224. https://doi.org/10.1016/j.icarus.2008.02.024

Nakajima, M., & Ingersoll, A. P. (2016). Controlled boiling on Enceladus. 1. Model of the vapor-driven jets. *Icarus*, *272*, 309–318. https://doi.org/10.1016/j.icarus.2016.02.027

Neveu, M., Anbar, A. D., Davila, A. F., Glavin, D. P., MacKenzie, S. M., Phillips-Lander, C. M., et al. (2020). Returning samples from Enceladus for life detection. *Frontiers in Astronomy and Space Sciences Astrobiology*, *7*, 26. https://doi.org/10.3389/fs-pas.2020.00026

Neveu, M., Desch, S. J., Shock, E. L., & Glein, C. R. (2015). Prerequisites for explosive cryovolcanismn on dwarf planet-class Kuiper belt objects. *Icarus*, *264*, 48–64. https://doi.org/10.1016/j.icarus.2014.03.043

Nimmo, F., Spencer, J. R., Pappalardo, R. T., & Mullen, M. E. (2007). Shear heating as the origin of the plumes and heat flux on Enceladus. *Nature*, *447*(7142), 289–291. https://doi.org/10.1038/nature05783

NIST. (2023). *NIST Chemistry WebBook* (Vol. 69). NIST Standard Reference Database Number. https://doi.org/10.18434/T4D303

Ono, M., Mitchell, K., Parness, A., Carpenter, K., Iacoponi, S., Simonson, E., et al. (2018). Enceladus vent explorer concept. In V. Badescu & K. Zacny (Eds.), *Outer solar system*. Springer. https://doi.org/10.1007/978-3-319-73845-1_13

Pankine, A. A. (2023). Numerical simulations of heat exchange and vapor flow in ice fractures on Enceladus. *Icarus*, *401*, 115584. https://doi.org/10.1016/j.icarus.2023.115584

Perera, L. J., & Cockell, C. S. (2023). Dispersion of bacteria by low-pressure boiling: Life detection in Enceladus' plume material. *Astrobiology*, *23*(3), 269–279. https://doi.org/10.1089/ast.2022.0009

Perry, M. E., Teolis, B. D., Hurley, D. M., Magee, B. A., Waite, J. H., Brockwell, T. G., et al. (2015). Cassini INMS measurements of Enceladus plume density. *Icarus*, *257*, 139–162. https://doi.org/10.1016/j.icarus.2015.04.037

Peter, J. S., Nordheim, T. A., & Hand, K. P. (2024). Detection of HCN and diverse redox chemistry in the plume of Enceladus. *Nature Astronomy*, *8*(2), 164–173. https://doi.org/10.1038/s41550-023-02160-0

Porco, C. C., DiNino, D., & Nimmo, F. (2014). How the geysers, tidal stresses, and thermal emission across the south polar terrain of Enceladus are related. *The Astronomical Journal*, *148*(3), 45. https://doi.org/10.1088/0004-6256/148/3/45

Porco, C. C., Helfenstein, P., Thomas, P. C., Ingersoll, A. P., Wisdom, J., West, R., et al. (2006). Cassini observed the active south polar of Enceladus. *Science*, *311*(5766), 1393–1401. https://doi.org/10.1126/science.1123013

Portyankina, G., Esposito, L. W., Aye, K. M., Hansen, C. J., & Ali, A. (2022). Modeling the complete set of Cassini's UVIS occultation observations of Enceladus' plume. *Icarus*, *383*, 114918. https://doi.org/10.1016/j.icarus.2022.114918

Postberg, F., Kempf, S., Schmidt, J., Brilliantov, N., Beinsen, A., Abel, B., et al. (2009). Sodium salts in E-ring ice grains from an ocean below the surface of Enceladus. *Nature*, *459*(7250), 1098–1101. https://doi.org/10.1038/nature08046

Postberg, F., Schmidt, J., Hillier, J., Kempf, S., & Srama, R. (2011). A salt-water reservoir as the source of a compositionally stratified plume on Enceladus. *Nature*, *474*(7353), 620–622. https://doi.org/10.1038/nature10175

Rabinovitch, J., Scamardella, J., Mitchell, K., & Cable, M. (2024). Supplementary Information for Mitchell and Rabinovitch et al., A proposed model for cryovolcanic activity on Enceladus driven by volatile exsolution [Dataset] [Software]. *Mendeley Data, V2*. https://doi.org/10.17632/kkhs9zr69y.2

Reh, K., Spilker, L., Lunine, J. I., Waite, J. H., Cable, M. L., Postberg, F., & Clark, K. (2016). Enceladus Life Finder: The search for life in a habitable moon. *IEEE Aerospace Conf*. https://doi.org/10.1109/AERO.2016.7500813

Rudolph, M. L., Manga, M., Walker, M., & Rhoden, A. R. (2022). Cooling crusts create concomitant cryovolcanic cracks. *Geophysical Research Letters*, *49*(5), e2021GL094421. https://doi.org/10.1029/2021gl094421

Sander, R. (2023). Compilation of Henry's law constants (version 5.0.0) for water as solvent. *Atmospheric Chemistry and Physics*, *23*(19), 10901–12440. https://doi.org/10.5194/acp-23-10901-2023

Schmidt, J., Brilliantov, N., Spahn, F., & Kempf, S. (2008). Slow dust in Enceladus' plume from condensation and wall collisions in tiger stripe fractures. *Nature*, *451*(7179), 685–688. https://doi.org/10.1038/nature06491

Shock, E. L., Helgeson, H. C., & Sverjensky, D. A. (1989). Calculation of the thermodynamic and transport properties of aqueous species at high pressures and temperatures: Standard partial molal properties of inorganic neutral species. *Geochimica et Cosmochimica Acta*, *53*(9), 2157–2183. ISSN 0016-7037. https://doi.org/10.1016/0016-7037(89)90341-4

Spahn, F., Schmidt, J., Albers, N., Hörning, M., Makuch, M., Seiß, M., et al. (2006). Cassini dust measurements at Enceladus and implications for the origin of the E-ring. *Science*, *311*(5766), 1416–1418. https://doi.org/10.1126/science.1121375

Spencer, J. R., & Nimmo, F. (2013). Enceladus: An active ice world in the Saturn system. *Annual Review of Earth and Planetary Sciences*, *41*(1), 693–717. https://doi.org/10.1146/annurev-earth-050212-124025

Spencer, J. R., Pearl, J. C., Segura, M., Flasar, F. M., Mamoutkine, A., Romani, P., et al. (2006). Cassini encounters Enceladus: Background and the discovery of a south polar hot spot. *Science*, *311*(5766), 1401–1405. https://doi.org/10.1126/science.1121661

Stenberg, S. K., Velle, G., Pulg, U., & Skoglund, H. (2020). Acute effects of gas supersaturation on Atlantic salmon smolt in two Norwegian rivers. *Hydrobiologia*, *849*(2), 527–538. https://doi.org/10.1007/s10750-020-04439-z

Szirtes, T. (2007). *Applied dimensional analysis and modeling* (2nd ed.). Butterworth-Heinemann. https://doi.org/10.1016/B978-012370620-1.50005-8

Tait, S., Jaupart, C., & Vergniolle, S. (1989). Pressure, gas content and eruption periodicity of a shallow, crystallizing magma chamber. *Earth and Planetary Science Letters*, *92*(1), 107–123. https://doi.org/10.1016/0012-821x(89)90025-3

Teolis, B. D., Perry, M. E., Hansen, C. J., Waite, J. H., Porco, C. C., Spencer, J. R., & Howett, C. J. A. (2017). Enceladus plume structure and time variability: Comparison of Cassini observations. *Astrobiology*, *17*(9), 926–940. https://doi.org/10.1089/ast.2017.1647

Trumbo, S. K., & Brown, M. E. (2023). The distribution of CO_2 on Europa indicates an internal source of carbon. *Science*, *381*(6664), 1308–1311. https://doi.org/10.1126/science.adg4155

Tsou, P., Brownlee, D. E., McKay, C. P., Anbar, A., Yano, H., Altwegg, K., et al. (2012). Life: Life investigation for Enceladus a sample return mission concept in search for evidence of life. *Astrobiology*, *12*(8), 730–742. https://doi.org/10.1089/ast.2011.0813

Vance, S. D., & Brown, J. M. (2005). Layering and double-diffusion style convection in Europa's ocean. *Icarus*, *177*(2), 506–514. https://doi.org/10.1016/j.icarus.2005.06.005

Vance, S. D., Craft, K. L., Schock, E., Schmidt, B. E., Lunine, J., Hand, K. P., et al. (2023). Investigating Europa's habitability with the Europa Clipper. *Space Science Reviews*, *219*(81), 81. https://doi.org/10.1007/s11214-023-01025-2

Vergniolle, S. (1996). Bubble size distribution in magma chambers and dynamics of basaltic eruptions. Earth Planet. *Science*, *140*(1–4), 269–279. https://doi.org/10.1016/0012-821x(96)00042-8

Villanueva, G. L., Hammel, H. B., Milam, S. N., Kofman, V., Faggi, S., Glein, C. R., et al. (2023). JPWST molecular mapping and characterization of Enceladus' water plume feeding its torus. *Nature Astronomy*, *7*(9), 1056–1062. https://doi.org/10.1038/s41550-023-02009-6

Villanueva, G. L., Hammel, H. B., Milam, S. N., Faggi, S., Kofman, V., Roth, L., et al. (2023). Endogenous CO2 ice mixture on the surface of Europa and no detection of plume activity. *Science*, *381*(6664), 1305–1308. https://doi.org/10.1126/science.adg4270

Waite, J. H., Combi, M. R., Ip, W. H., Cravens, T. E., McNutt Jr, R. L., Kasprzak, W., et al. (2006). Cassini ion and neutral mass spectrometer: Enceladus plume composition and structure. *Science*, *311*(5766), 1419–1422. https://doi.org/10.1126/science.1121290

Waite, J. H., Glein, C. R., Perryman, R. S., Teolis, B. D., Magee, B. A., Miller, G., et al. (2017). Cassini finds molecular hydrogen in the Enceladus plume: Evidence for hydrothermal processes. *Science*, *356*(6334), 155–159. https://doi.org/10.1126/science.aai8703

Waite, J. H., Lewis, W. S., Magee, B. A., Lunine, J. I., McKinnon, W. B., Glein, C. R., et al. (2009). Liquid water on Enceladus from observations of ammonia and 40Ar in the plume. *Nature*, *460*(7254), 487–490. https://doi.org/10.1038/nature08153

Waite, J. H., Magee, B., Brockwell, T., Zolotov, M. Y., Teolis, B., & Lewis, W. S. (2011). Enceladus' plume composition. *EPSC Abstracts*, *61*. EPS-DPS2011-61-4, EPS-DPS Joint Meeting 2011.

Watson, Z. T., Han, S. W., Keating, E. H., Jung, N.-H., & Lu, M. (2014). Eruption dynamics of CO2-driven cold-water geysers: Crystal, Tenmile geysers in Utah and Chimayó geyser in New Mexico. *Earth and Planetary Science Letters*, *408*, 272–284. https://doi.org/10.1016/j.epsl.2014.10.001

Weitkamp, D. E., & Katz, M. (1980). A review of dissolved gas supersaturation literature. *Transactions of the American Fisheries Society*, *109*(6), 659–702. https://doi.org/10.1577/1548-8659(1980)109<659:arodgs>2.0.co;2

Wilson, L. (1980). Relationships between pressure, volatile content and ejecta velocity in three types of volcanic explosion. *Journal of Volcanology and Geothermal Research*, *8*(2–4), 297–313. https://doi.org/10.1016/0377-0273(80)90110-9

Wilson, L., & Head, J. W. (1981). Ascent and eruption of basaltic magma on the Earth and Moon. *Journal of Geophysical Research*, *86*(B4), 2971–3001. https://doi.org/10.1029/jb086ib04p02971

Wilson, L., Sparks, R. S. J., & Walker, G. P. L. (1980). Explosive volcanic eruptions – IV. The control of magma properties and conduit geometry on eruption column behaviour. *Geophysical Journal of the Royal Astronomical Society*, *63*(1), 117–148. https://doi.org/10.1111/j.1365-246x.1980.tb02613.x

Wood, A. B. (1941). *A textbook of sound*. G. Bell and Sons.

Woodbury, L. A. (1942). A sudden mortality of fishes accompanying a supersaturation of oxygen in Lake Waubesa, Wisconsin. *Transactions of the American Fisheries Society*, *71*(1), 112–117. https://doi.org/10.1577/1548-8659(1941)71[112:asmofa]2.0.co;2

Wylie, J. J., Helfrich, K. R., Dade, B., Lister, J. R., & Salzig, J. F. (1999). Flow localization in fissure eruptions. *Bulletin of Volcanology*, *66*, 423–440.

Yeoh, S. K., Li, Z., Goldstein, D. B., Varghese, P. L., Levin, D. A., & Trafton, L. M. (2017). Constraining the Enceladus plume using numerical simulation and Cassini data. *Icarus*, *281*, 357–378. https://doi.org/10.1016/j.icarus.2016.08.028

Yumoto, K., Cho, Y., Koyaguchi, T., & Sugita, S. (2023). Dynamics of a gas-driven eruption on Ceres as a probe to its interior. *Icarus*, *400*, 115533. https://doi.org/10.1016/j.icarus.2023.115533

Zhang, Y. (1996). Dynamics of CO2-driven lake eruptions. *Nature*, *379*(6560), 57–59. https://doi.org/10.1038/379057a0

Zhang, Y. (2000). Energetics of gas-driven limnic and volcanic eruptions. *Journal of Volcanology and Geothermal Research*, *97*(1–4), 215–231. https://doi.org/10.1016/s0377-0273(99)00164-x